ISSN 0869-5911, Petrology, 2024, Vol. 32, No. 3, pp. 307–336. © Pleiades Publishing, Ltd., 2024.

Fenner Trend and the Role of Fractional Crystallization and Ferrobasaltic Magma Immiscibility in Granophyre Petrogenesis: the Case of the Mesoproterozoic Valaam Sill in the Ladoga Graben, Karelia

A. A. Nosova[a, *], N. M. Lebedeva[a], A. A. Vozniak[a], L. V. Sazonova[a, b], I. A. Kondrashov[a], Y. O. Larionova[a], and E. V. Kovalchuk[a]

[a] *Institute of Geology of Ore Deposits, Petrography, Mineralogy, and Geochemistry, Russian Academy of Sciences, Moscow, Russia*

[b] *Geological Department, Lomonosov Moscow State University, Moscow, Russia*

**e-mail: nosova@igem.ru*

Received July 13, 2023; revised December 9, 2023; accepted January 18, 2024

Abstract—This paper presents the results of petrographical, mineralogical, geochemical, and isotope-geochemical studies of granophyres and host ferrogabbros, quartz ferromonzogabbros, quartz monzodiorites, and quartz monzonites in the Mesoproterozoic Valaam sill in the Ladoga Graben on the Karelian Craton. The sill is poorly layered: the ferrogabbros compose the lower part of the sill, the middle part consists of quartz gabbro-monzonites and quartz monzonites, while graphic leucogranites (granophyres) form a dense network of veins mainly in the upper part of the sill. Geochemical features of ferrogabbro, iron-rich composition of olivine and pyroxene, and low Ca composition of plagioclase indicate the evolution along the Fenner trend. The granophyres have petro- and geochemical characteristics of anorogenic alkaline granites, with negative Eu/Eu* = 0.15–0.49 and REE distribution patterns similar to those of granophyres of layered intrusions. All rocks of the sill have close Sr isotopic composition ($(^{87}Sr/^{86}Sr)_T$ = 0.7043–0.7066, and ε_{Nd} values ranging from −9.6 to −11.2. Model calculations show that fractional crystallization can lead the initial ferrogabbro melt into the immiscibility field. Ilmenite–magnetite–silicate microstructures have been identified in the ferrogabbro and ferromontzogabbro from the sill; similar microstructures in layered intrusions are considered as evidence for the immiscibility of Fe-rich and Si-rich liquids (Holness et al., 2011; Dong et al., 2013). The segregation of the high-silica melt may have occurred in an intermediate crustal chamber at around 350 MPa and 960°C; magma was supplied as crystalline mush at the sill emplacement level at around 70 MPa and acidic melt migrated through it. This melt underwent fractional crystallization and interacted with host minerals. At the level of sill emplacement, it crystallized under supercooling into granophyre aggregates. The example of the Valaam sill shows that when the Fenner fractionation reaches the final composition–-ferrogabbro, its further evolution with a conjugate decrease in SiO_2 and Fe contents can be related to the incomplete separation and mixing of Fe-rich melts and immiscibly split felsic melt. Such a mechanism can be implemented for the formation of the mafic part of AMCG-type massifs.

Keywords: granophyre, ferrogabbro, quartz monzonites, sill, AMCG-type massifs, layered intrusions, immiscibility, fractional crystallization, A-granites, Fennoscandia

DOI: 10.1134/S086959112470005X

INTRODUCTION

Felsic component of both layered intrusions and AMCG-type massifs is represented by A-type granites in association with anorthosites and Fe-rich mafic rocks: gabbros, gabbronorites (e.g., Wager and Brown, 1968; McBirney, 1996; Bonin, 2007; Shellnutt et al., 2009; Larin, 2011; Latypov et al., 2020). These granites have the high Fe, Ti, P, HFSE, and REE contents and crystallized at high temperatures, low H_2O content, and low oxygen fugacity (below QFM buffer) (Bonin, 2007; Foden et al., 2015)

The AMCG-type massifs are made up mainly of granites, which are characterized by the rapakivi textures and the occurrence of highly fractionated varieties (topaz leucogranites). The presence of composite dikes indicates the coexistence of acidic and basic magmas (Larin, 2011). The origin of granites in the AMCG-type massif remains controversial and is considered mainly in the framework of the following models: melting of the lower crust with appearance of mangerite and charnockite magmas under the impact of basalt melts (e.g., McLelland et al., 2010); fraction-

ation of ferrosyenites (jotuines), which represent partial melts from tholeiitic magma that underplated the crustal base (e.g., Frost and Frost; 1997), or differentiation of tholeiitic magmas (high-Al basalts formed through assimilation–fractional crystallization (AFC) of tholeiitic basalt) at the crustal base with formation of anorthosites and A-type felsic derivatives (e.g., Fred et al., 2020). Data on iron isotope composition indicate that A-type granites could be formed through the immiscibility of Fe-rich and Si-rich silicate melts (Zhu et al., 2015).

In layered massifs, acidic rocks are mainly represented by granophyres (e.g., Namur et al., 2010; Skursch et al., 2020 and references therein); their amount is variable but usually accounts for subordinate part of the intrusions. In particular, granophyres in the upper parts (UZ and UBSγ) of the Skaergaard intrusion account for ~ 5% (Bindeman et al., 2008 and references therein). Granophyres usually occur as separate lenses, sills, dikes, and veins. The origin of granite component in layered massifs has been hotly debated for a long time. Since fractionation of melts in these massifs usually follow a tholeiitic trend, intermediate rocks occur in subordinate amount. This emphasizes the bimodal rock distribution and makes it possible to study the massifs to address the "Daly gap" (e.g., Shellnutt et al., 2009).

Fractionation of basaltic melts along the tholeiitic (Fenner) trend suggests Fe accumulation at almost constant SiO_2 in melt with formation of ferrogabbro as a final derivative (Fenner, 1929). In some cases, this trend continues subsequently or drastically, producing melts with decreasing Fe content at increasing SiO_2 content, up to formation of ultra-high silica melts, i.e., formally follows the Bowen trend (Bowen-like trend, Lesher et al., 2023).

The nature of this last segment of the trend is controversial. Three main points of view are proposed to explain the genesis of felsic melts in layered intrusions. According to the first point, felsic residual melts could be produced by a closed-system fractional crystallization of initial basaltic and ferrobasaltic magmas. This point of view is confirmed by geological and petrological observations (e.g., Namur et al., 2010; Skursch et al., 2020), as well as by thermodynamic modeling (e.g., Vantongeren et al., 2010; Shellnutt et al., 2009). Second, felsic component could represent a partial crustal melt produced by heat from mafic melts, which is confirmed by the Sr, Nd, and Pb isotope data (e.g., Troll et al., 2021). Recently, increasingly more evidences have been obtained on the formation of felsic component through the immiscibility between Fe-rich and Si-rich melts, which was caused by the fractionation crystallization of basaltic melt along a tholeiitic (Fenner) trend. This mechanism of granophyre formation follows from observations of natural and experimental microstructures in the rocks of layered intrusions (e.g., Holness et al., 2011; Honour et al., 2019), mineral geochemistry (e.g., VanTongeren and Mathez, 2012), melt inclusions in minerals (e.g., Jakobsen et al., 2005), as well as from experimental works reproducing Fe–Si melt immiscibility (e.g., Charlier and Grove, 2012; Zhang et al., 2023; Lino et al., 2023), and thermodynamic modeling (e.g., Fischer et al., 2016; Lino et al., 2023).

This paper is dedicated to the felsic rocks in the Mesoproterozoic Valaam sill made up of Fe-rich derivatives (ferrogabbro, ferrogabbromonzonites, and others) and granophyre veins. This sill spatially associates with the large AMCG-type Salmi massif, but is separated from it in time by no less than 70 Ma (Neymark et al., 1994; Amelin et al., 1997; Rämö et al., 2001). The origin of felsic melt that formed the granophyre veins in the sill remains under question (Sviridenko and Svetov, 2008; Frank-Kamenetsky, 1998): whether it is derivative of partial melting of crustal protolith or was produced by fractional crystallization of basaltic melt?

Crystallization and post-crystallization history of the sill in a stable intracontinental setting made it possible to freeze microtexture and microstructure of rapidly proceeding processes, for instance, traces of ascending fluid bubble jets or granophyre pipes (Sviridenko and Svetov, 2008), which highlight the melt evolution in a shallow chamber. In many other cases, their traces have been erased by subsequent deformation.

The aim of this work was to establish the mechanism and conditions of origin of granophyres of the Valaam sill based on the petrographical, mineralogical, geochemical, and isotope geochemical studies of the granophyres and host rocks. This sill with a unique preservation of crystallization structures and textures is considered as a fossilized natural laboratory for the study of melt evolution in a shallow chamber. Our studies show that the immiscibility of silicate melts played a significant role in the origin of felsic component of the sill. In addition, given the geological position of the sill as recording the final episode of the large-scale AMCG-type magmatism at the East European craton, deciphering of mechanisms of its formation and revealing the role of melt immiscibility expand understanding the evolution of granite rapakivi complexes and emphasize their similarity with layered intrusions, which is of great significance for estimating their ore potential.

GEOLOGICAL BACKGROUND OF THE VALAAM SILL

Geological Position of the Vallam Sill

The AMCG-type massifs of the East European craton were formed within 1.67–1.45 Ga: large massifs were formed at the early stage 1.67–1.49 Ga (Riga, Vyborg, and Salmi) mainly in the central part of the Svecofennian domain, while small granite and gabbro

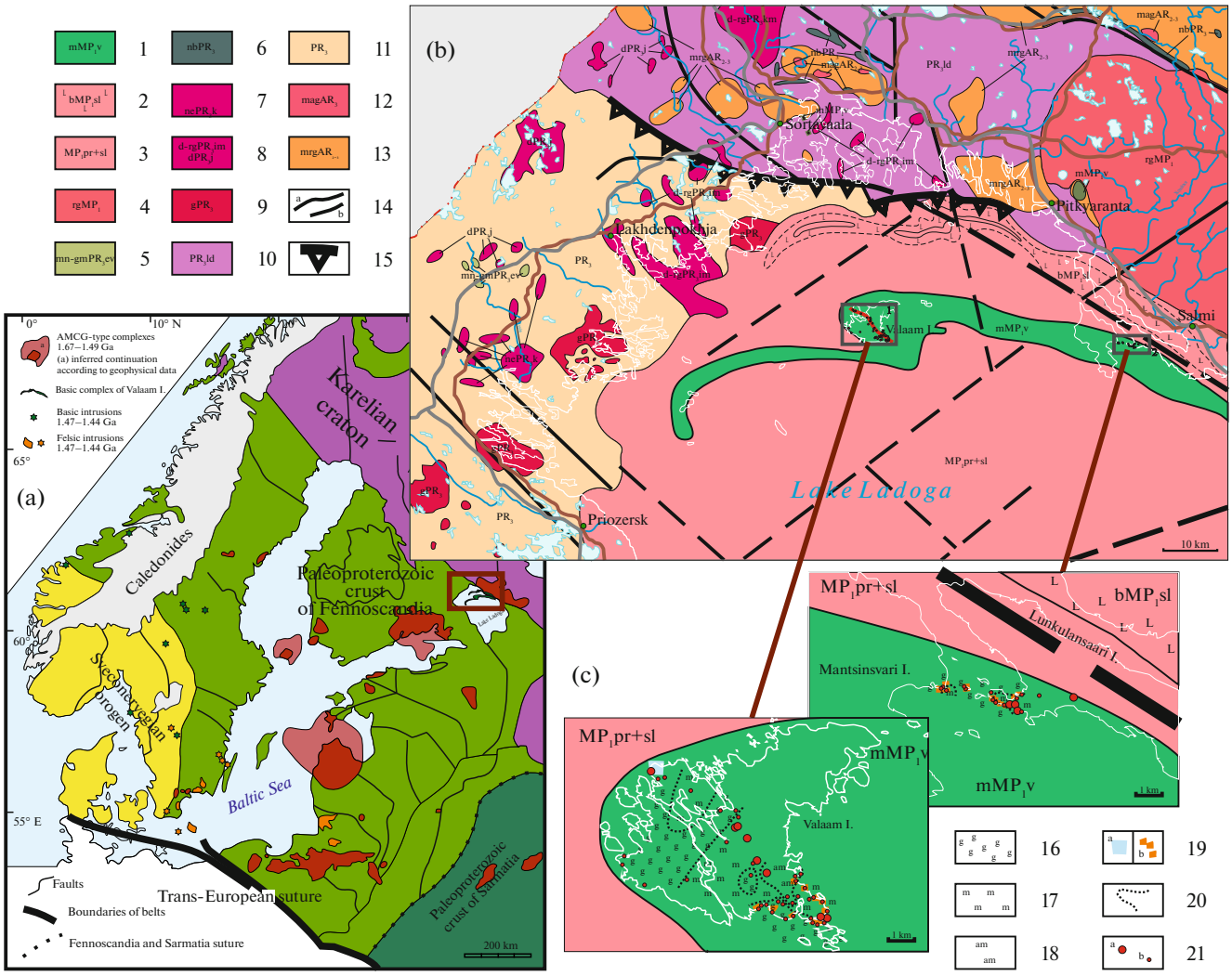

Fig. 1. (a) Geological position of the Valaam sill in structures of the northwestern East European Craton modified after (Brander and Söderlund, 2007) and (Grabarczyk et al., 2023). Area distinguished by box is shown in Fig. (b). (b) Geological scheme of the Northern Ladoga region shows the position of the Valaam sill within the Ladoga graben in the junction zone of the Karelian craton and Svecofennian orogen. (1, 2) *volcanic association of the Ladoga graben*: (1) Valaam sill, ferrogabbro, quartz ferromonzogabbro, monzodiorite, quartz monzonite, and graphic leucogranites (μMP_1v); (2) ferrobasalts, Salmi Formation (βMP_1sl); (3) siltstones, sandstones, Priozersk and Salmi formations, (MP_1pr+sl); (4) AMCG-type Salmi massif ($\rho\gamma MP_1$). (5–11) *Svecofennian orogenic domain*: (5) Elisenvaara–Vuoksa monzogabbro–monzonite–syenite–granite complex ($\mu\nu$-$\gamma\mu PR_3ev$); (6) diorite–basite complex ($\nu\beta PR_1$); (7) Kurkijoki norite–enderbite (νePR_1k), and (8) Impiniemi and Yakkima diorite–tonalite ((δ-$\rho\gamma PR_1im$ δPR_1j) complexes; (9) undivided granites (γPR_3); (10) Ladoga Group, biotite gneisses, quartz–mica schists, and other metamorphic rocks (PR_1ld); (11) Isojarvi metamorphic sequence, metatuffites (PR_1); (12) synorogenic undivided plutonic complexes, migmatites, and granites ($m\alpha\gamma AR_3$); (13) migmatite–plagiogranite complexes of the Karelian Craton ($m\rho\gamma AR_{2\text{-}3}$); (14) faults: (a) proved, (b) inferred; (15) Mejeri Thrust. (c) studied area. Geological background modified after (Maksimov et al., 2015; Stepanov et al., 2004); geological schemes of detailed areas on islands are shown in boxes (b): (16) ferrogabbros; (17) quartz monzonites, (18) amphibole quartz monzonites; (19) veins: (a) in quartz monzonites, (b) graphic leucogranites; (20) contours of rock varieties, (21) observation points: (a) used in this work and in Supplementary 1, ESM_1, (b) others.

massifs, dolerite dike swarms, and the Valaam sill were formed at the periphery of the Svecofennian domain at the late stage 1.38–1.45 Ga (Fig. 1a) (Brander and Söderlund, 2007; Johansson et al., 2022, Grabarczyk et al., 2023).

The Valaam sill is located in the Ladoga graben, which is characterized by the composite inner structure with alternation of local horsts and depressions (Amantov et al., 1996; Artemieva and Shulgin, 2015); the graben is filled with the Meso- and Neoproterozoic sequence of terrigenous and subordinate carbonate sediments from 350 to 600 m thick (e.g., Kuptsova et al., 2011). Magmatic rocks were not found in the western part of the graben. Sedimentary sequences filling the eastern part of the Ladoga graben host volcanic and subvolcanic magmatic rocks represented by

flows of ferrobasalts and basaltic andesites, ferrodolerite dikes, Khopunvaara subvolcanic body (neck), and Valaam sill (Fig. 1b).

In the northeastern Ladoga region, ferrobasalts compose two lava flow sequences up to 155 m thick separated by a sedimentary unit. Ferrodolerite dikes up to 25 m thick traced by strike for 7 km (Lubnina et al., 2010) compose N–NW trending swarm in the Northern Ladoga region among Svecofennian metamorphic rocks. The rocks of the Valaam sill contain ferrobasaltic xenoliths, which were found on Vil'yamoi Island (Sviridenko and Svetov, 2008). The ferrobasalts are localized among graben sediments, the basal horizon of which contains zircon with the youngest age of 1477 ± 8 Ma (Kuptsova et al., 2011).

The Valaam sill defines U-Pb baddelleyite dates of 1459 ± 3 and 1457 ± 2 Ma (Ramö et al., 2001). The large Mesoproterozoic (1.57–1.53 Ga) Salmi granite rapakivi–quartz–diorite–anorthosite–gabbronorite massif is confined to the eastern wall of the graben (Larin, 2011).

Structure of the Valaam Sill

The rocks of the Valaam sill compose the Valaam–Salmi island range in the northern part of Lake Ladoga (Fig. 1b). The area of the sill is estimated at ~2000 km^2 (Frank-Kamenetsky, 1998), but, given the geophysical data, it could be much greater and reach ~16 thou. km^2 (Svetov and Sviridenko, 1995). The thickness of the sill is estimated as 200 m (Svetov and Sviridenko, 1995).

The sill shows no clear layering (e.g, Sviridenko and Svetov, 2008). Nevertheless, there are no doubts that ferrogabbros are confined to the lower part of the sill. They were established both on Valaam Island in the central part and on Lunkulunsaari Island, in the eastern part of the sill, and their exposed thickness above water level reached a few to tens of meters. In the central part (Valaam I.), the sill is composed of ferrogabbro and ferrogabbromonzonite, which contain extended lenticular interlayers of massive quartz monzonites tens meters thick. In the northeastern direction, toward the inferred sill roof, the fraction of monzonites increases (Fig. 1c). The monzonites are intersected by a dense network of red granophyre veins (Fig. 2). In the eastern part, on the Lunkulunsaari and Mantinsaari islands, the massive monzonites are less common, while granophyre veins cut across ferrogabbro and quartz ferromonzogabbro (Fig. 1c).

Position and Characteristics of the Granite Veins in the Valaam Sill

Ferrogabbro and monzonite of the Valaam sill contain granophyre veins of two main generations: early gray veins up to 3 cm thick and late red veins 20–30 cm thick; the former occur in the lower part of the sill, while the latter, in its upper part; in addition, there are granophyre pipes up to 80 cm across (Sviridenko and Svetov, 2008). Our observations in general confirm this pattern (Fig. 2).

"Gray" veinlets are composed of fine-grained monzonite with granophyre areas (see Petrography section). Such veinlets are scarce; NS-trending veinlet 5 cm thick was found among ferrogabbro in the northwestern part of Valaam Island (Moskovskii Cape, sample 21C-22) (Fig. 2c).

The "red" veins are widespread. We studied them in the eastern–southeastern part of Valaam Island and on the Lunkulansaari and Mantinsaari Islands. The veins are made up of graphic leucogranite (see Petrography section), while host rocks are massive monzonite on Valaam Island and additionally quartz monzogabbro on other islands (Figs. 2a, 2b, 2d). The veins have both vertical (Figs. 2a, 2b), and very low-angle, subhorizontal dip (Fig. 2d). According to (Sviridenko and Svetov, 2008), granophyre veins strike mainly NW and NE (330°–60°); according to our observations, NE and NS strikes are predominant. The thickness of the veins varies from 2–3 to 20 cm, the lower angle veins are usually thicker. In the regions saturated in the veins (for instance, the cape of Ladozhskii on Valaam Island, the western termination of Lunkulunsaari Island), there are up to 10 veins per 100 m of section. The veins are characterized by the orthogonal junction and geniculate bends.

In places where granophyre veins are concentrated, granophyre pipes are found (Figs. 2e, 2f). The pipes could be connected with veins and are accompanied by halo of alkaline feldspar in the host rocks. Similar granophyre pipes representing pathways for the transportations of felsic melt through unconsolidated cumulate were described in some layered intrusions, for instance, in the Skaergaard massif (Larsen, 2008). The detailed description of granophyre pipes in the Valaam sill is given in (Sviridenko and Svetov, 2008).

The clusters of the granophyre veins are accompanied by the 2–3 cm thick quartz–carbonate veins (Valaam and Mantinsaari islands).

PETROGRAPHY

The Valaam sill is made up of ferrogabbro, quartz ferromonzogabbro and quartz ferromonzodiorite, quartz monzonite, and graphic leucogranite (granophyre). The quartz ferromonzogabbro and quartz ferromonzodiorite are transitional rocks from ferrogabbro to quartz monzonite.

The ferrogabbro is the coarse-grained rock with porphyritic subophitic texture and elements of cumulate, poikilitic textures. It consists of large euhedral clilnopyroxene crystals (up to 35%) frequently rimmed by orthopyroxene, which are saturated in ilmenite inclusions and to lesser extent in Ti-magnetite; subhedral olivine crystals (10%), which can be

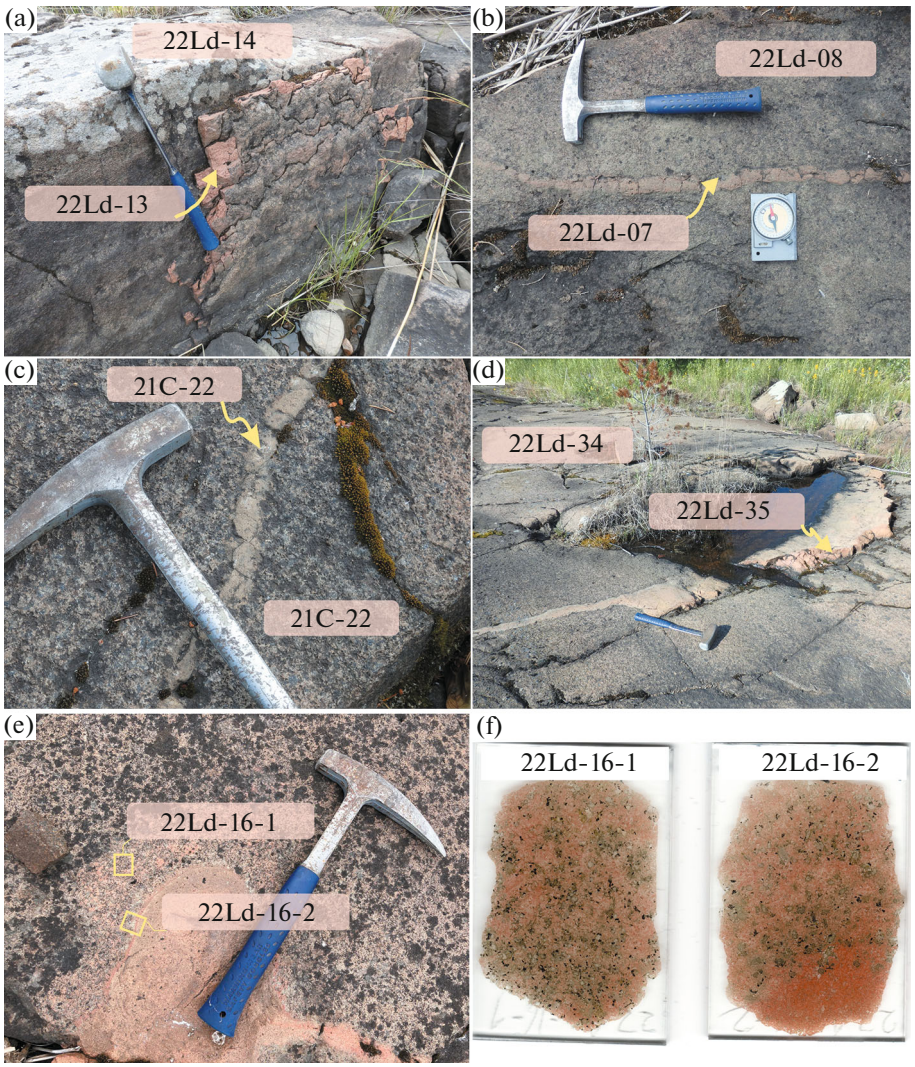

Fig. 2. Veins of graphic leucogranite and quartz monzonite in the Valaam sill: (a) and (b) veins in quartz ferromonzogabbro on Lunkulunsaari Island; (c) quartz monzonite vein in ferrogabbro from the northwestern part of Valaam island; (d) low-angle leucogranite vein in the quartz ferromonzogabbro in the southeastern part of Valaam Island; (e) pipe of the graphic leucogranite in quartz ferromonzogabbro, Lunkulunsaari Island; (f) scans of polished thin sections, with sampling sites indicated in Fig. 2e.

also overgrown by orthopyroxene (Fig. 3a), and long tabular plagioclase crystals (up to 40%). Large ilmenite grains frequently occur as intergrowths with silicate phases (amphibole, biotite, and others), are surrounded by magnetite and replaced by titanite, account for up to 10 wt %. Apatite (up to 5 wt %) occurs as individual extended crystals and inclusions in clinopyroxene and olivine. There are also single biotite flakes (Fig. 3a).

The quartz ferromonzogabbro and quartz monzodiorites. The transitional varieties contain quartz and K–Na feldspar. The quartz ferromonzogabbro has subophitic texture with large clinopyroxene crystals and tabular plagioclase. KFsp–quartz granophyric aggregate fills interstices between plagioclase crystals (Fig. 3b). Plagioclase grains are rimmed by K-feldspar, while clinopyroxene is surrounded by amphibole rim; in addition, clinopyroxene is subsequently replaced by biotite and chlorite (Fig. 3d). These rocks contain ilmenite–amphibole intergrowths with magnetite rims; in these intergrowths, the ilmenite occurs as worm-like lamellae in silicate mineral, showing eutectoid appearance. The intergrowths occupy ~ 5 vol % (Fig. 3a).

The quartz monzodiorite shows an increase of granophyre mass. Clinopyroxene grains are frequently present as relicts in amphibole (ferroedenite). In some cases, amphibole completely replaces clinopyroxene. In some grains, amphibole rim is preserved, while the core is replaced by a mixture of biotite, chlorite, tiny quartz, and carbonate. K-feldspar forms not only rims on plagioclase, but also individual crystals. Ilmenite is

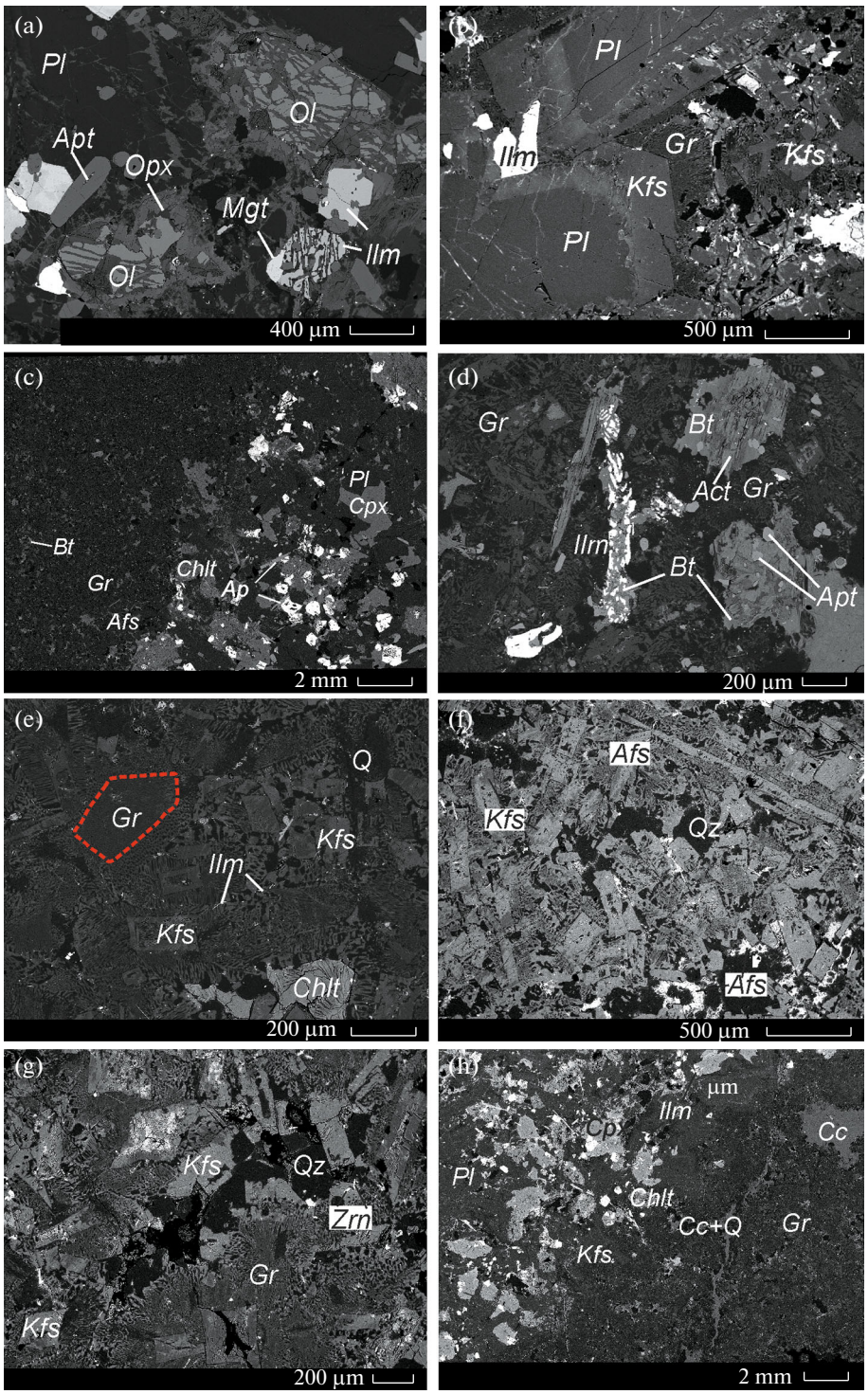

replaced by titanite. Granophyre aggregate surrounds K-feldspar, and inherits their morphology. Some interstices contain pocket-like aggregates (micromiarole) consisting of euhedral quartz (up to 5 mm) and xenomorphic carbonate grains, biotite flakes, as well as tiny crystals of zircon and apatite needles and small veinlets of carbonate.

The quartz monzonite and amphibole quartz monzonite have medium-grained texture (grain size up to 2.5 cm), while granophyres are developed in inter-

Fig. 3. BSE images of rocks of the Valaam sill. (a) ferrogabbro, Fe-rich olivine with orthopyroxene fringe; symplectitic ilmenite–magnetite intergrowths as well as separate grains of magnetite and apatite are well seen (sample 21C-21); (b) quartz ferromonzogabbro. K-Fsp grows onto plagioclase grains, while interstices between large feldspar grains are filled with granophyre intergrowths of K-feldspar and quartz (sample 22LD-06); (c) contact zone between quartz ferrogabbro (on the right) and granophyre part of the vein monzonite sample (on the left). At the contact, K-Feldspar grows on the plagioclase grains and clinopyroxene is replaced by chlorite and biotite (sample 21C-22); (d) contact between vein of graphic leucogranite and quartz ferrogabbro. Round clinopyroxene grains are replaced by biotite and actinolite; the rock contains symplectite-like ilmenite–amphibole intergrowths, apatite is confined to the ilmenite and replaced clinopyroxene grains. Interstices are filled with granophyre aggregate (sample 22LD-16); (e) graphic leucogranite, grains of feldspar are completely or partly replaced by fine-grained granophyre intergrowths (GR), which are overgrown by coarser grained granophyre intergrowths, with preserved patchy relicts of the feldspar (sample 22LD-06); (f) graphic leucogranites, with alkali feldspar and quartz granophyre intergrowths developed between feldspar laths, late xenomorphic masses of quartz and biotite are developed between the granophyre intergrowths (sample 22LD-13); (g) graphic leucogranite vein, filled with quartz and K-Fsp, gently grading into granophyre intergrowths of K-feldspar and quartz (sample 22LD-06); (h) contact zone between graphic leucogranite and quartz ferrogabbro. At the contact between the ferrogabbro made up of plagioclase and pyroxene, K-Fsp grows on plagioclase and clinopyroxene is replaced by amphibole; granophyre is intersected by veinlet filled with quartz and carbonate; the granophyre also contains micromiarole filled with carbonate (sample 22LD-06).

stices. The rock consists of plagioclase (30%), K-Na feldspar (25%), clinopyroxene (5–10%), amphibole (10–15%), apatite (5%), intergrowths of ilmenite with magnetite (5%), and quartz (15%), as well as accessory titanite, zircon, and baddeleyite.

These rocks demonstrate more intense development of K-Fsp rims around plagioclase, as well as replacement of plagioclase grains by K-Na feldspar and granophyre intergrowths. The granophyre aggregate amounts up to 20%.

Clinopyroxene crystals have mainly xenomorphic appearance, are frequently rimmed by amphibole; individual amphibole grains are also present. At the contact of monzonite and graphic leucogranite (granophyre), clinopyroxene is replaced by chlorite and biotite. Ilmenite–silicate intergrowths are usually surrounded by magnetite rims, frequently they are intergrown with elongated apatite. Near the contact with granophyres, ilmenite is replaced by titanite (Fig. 3c). The rock contains pockets composed of euhedral quartz, carbonate, chlorite, titanite, apatite, and ilmenite.

Vein monzonites are finer grained, plagioclase laths reach 1 mm, clinopyroxene is practically absent, while mafic minerals are represented by only amphibole. There are also granophyre areas with relatively large (up to 2 mm) euhedral quartz, chlorite, biotite, and titanite.

The graphic leucogranite (granophyre) is massive rock with fine to medium-grained porphyritic texture, and granophyre, massive groundmass. The rock consists of K- and K–Na feldspar (45%), quartz (40%), albite (5%), and chloritized biotite (5%), and contains numerous tiny (up to 50 μm) zircon grains, which occasionally reach 5% (Fig. 4). Accessory minerals are also apatite, amphibole, ilmenite, baddeleyite, monazite, and titanite. Some areas of granophyre aggregate are developed conformably with morphology of KFsp crystals (Fig. 3e). Small xenomorphic domains filled with mica and chlorite likely represent pseudomorphs after amphibole or clinopyroxene (Fig. 3f). Granophyre texture in this rock is extremely diverse and varies widely in size of intergrowths and composition of K–Na feldspar, locally reaching pure K-Fsp composition (Fig. 3f). Some domains (micromiarole) are composed of late magmatic aggregate of euhedral quartz and K feldspar, as well as veinlets filled with KFsp, carbonate, albite, and quartz (Fig. 3g). It should be noted that many zircon grains are also confined to the carbonate segregations.

In addition to veins, graphic leucogranite composes pipes (Figs. 2e, 2f). They have reaction relations with host rocks, and their mineral composition insignificantly differs, first of all, in the higher contents of H_2O-bearing minerals (chlorite, actinolite, biotite) compared to vein leucogranites. The content of hydrous minerals can reach 15 vol %. Thereby, only these leucogranites are characterized by the presence of intergrowths of ilmenite and biotite (Fig. 3d), as well as replacement of ilmenite by titanite.

Quartz microstructures. Quartz monzonite and graphic leucogranite of the Valaam sill contain diverse quartz microstructures, which can be subdivided into isolated grains and grapnophyre aggregate. Quartz is also present as irregular inclusions in feldspar.

The isolated grains are peculiar in the well-shaped prismatic and dipyramidal facets and relatively large sizes 50–500 μm across (Fig. 4). Single grains are surrounded by feldspar crystals or joins the granophyre aggregate, or grains (up to 3–5 grains) are grouped into clusters forming short chains (Fig. 4).

Dyck and Holness (2022) suggest that such chained quartz clusters are formed in the melt, when quartz grains move freely and rotate relative each other; corresponding conditions in felsic melt could exist until the fraction of crystals reaches 0.2–0.3.

METHODS

Sampling and Preparation

Samples for studies were collected from veins of graphic leucogranite and quartz monzonite, and from host rocks along profile intersecting the Valaam sill from the SW to SE across strike of cryptic layering of

the sill (Fig. 1c). In total, we have analyzed 27 samples (see Supplementary[1] 1, ESM_1), from which polished thin sections mounted in epoxy resin and samples for chemical and isotope analysis were prepared. Optical, microprobe, and geochemical studies were carried out for all samples, while Sr and Nd isotope compositions were analyzed in ten samples. A detailed description of the methods is given in Supplementary 2, ESM_2.

Scanning electron microscopy and EDS. The study of rock texture was carried out on a Jeol JSM-6480LV scanning electron microscope at the Geological Faculty of the Lomonosov Moscow State University and a Jeol JSM-5610LV at the Institute of Geology of Ore Deposits, Petrography, Mineralogy, and Geochemistry (IGEM RAS, Moscow).

Cathodoluminescence. The cathodoluminescence (CL) study was carried out at the IGEM RAS using a Cameca MS-46 electron microprobe microanalyzer equipped with high-resolution Videoscan 285 digital camera.

Electron-probe microanalysis (EPMA). Mineral compositions were analyzed on a JEOL JXA-8200 wavelength spectrometer at the IGEM RAS. The analysis was carried out at an accelerating voltage of 20 kV, beam current of 20 nA, and beam diameter of 3 μm.

The Ti content in quartz was measured using the same instrument at the IGEM RAS at an accelerating voltage of 20 kV, beam current of 300 nA. The peak and background counting times of Ti (Ka, PETH) were 200 and 100 s, respectively. The detection limit (3 σ) is 15 ppm.

LA-ICP-MS. The Ti content in quartz was also determined using LA-ICP-MS on a high-resolution Element-XR mass spectrometer with ionization in inductively coupled plasma with UP-213 laser device at the Vernadsky Institute of Geochemistry and Analytical Chemistry (GEOKHI RAS, Moscow). Obtained data were processed in a Glitter software (Van Achterbergh et al., 2001).

XRF. Contents of major components were determined by X-ray fluorescence on a PW-2400 (Philips Analytical B.V.) spectrometer at the IGEM RAS.

ICP-MS. Concentrations of trace elements in 22 samples were determined by inductively coupled plasma mass spectrometry (ICP-MS) at the Institute of Microelectronics Technology and High-Purity Materials (Chernogolovka) using analytical procedure (Karandashev et al., 2017).

Sr and Nd isotope analysis. The Sr and Nd isotope compositions in whole rock samples were determined by TIMS at the Laboratory of Isotope Geochemistry and Geochronology of IGEM RAS.

Geothermobarometry. Crystallization conditions of ferrogabbro and quartz monzodiorite were determined using mineral geothermometers and geobarometers.

For clinopyroxene–melt equilibrium conditions, temperature and pressure were calculated with clinopyroxene–melt geobarometer using equations 30, 31, and 33 (Putirka, 2008). The errors in geothermometers and geobarometers are estimated as ±42°C for equation 33 and ±2.9 and ±3.6 kbar for equations 31 and 30, respectively. The temperatures of coexisting feldspars were calculated using equation 27b with error of ± 30°C. Temperature and oxygen fugacity for coexisting magnetite and ilmenite were estimated using the Uvsp–Ilm thermooxybarometer, with errors of ±70°C and ± 0.4 log u. respectively (Sauerzapf et al., 2008).

The temperature and pressure of ferroedenite crystallization both in separate crystals and in wide rims around clinopyroxene were calculated after (Ridolfi, 2021). Application of this method for separate crystals (with determination of both core and rim compositions) and wide ferroedenite rims around clinopyroxene is justified by fulfilment of two main criteria for their equilibria with melt (Ridolfi et al., 2010): homogeneity of amphibole compositions in all petrographic positions (Al^{IV} = 0.87 ± 0.12 apfu and K_A = 0.19 ± 0.01 apfu, N = 22) and euhedral habit of separate crystals and rims. The errors are ±22°C for temperature and ±12% (1 δ) for pressure, but in our case the error could be even higher due to the lower Mg contents in amphiboles compared to the amphibole compositions used for calibration of the geothermobarometer. Estimated *P-T* parameters for amphibole are within calibrated values (Ridolfi, 2021).

The temperature and pressure of quartz crystallization based on the Ti concentration (TitaniQ) were calculated using two models: HA12 (Huang and Audétat, 2012) and Z20 (Zhang et al., 2020). Model HA12 was calibrated within 600–800°C and 1–10 kbar for Ti partitioning between quartz and Ti-bearing water fluid, however, is recommended for magmatic rocks (Huang and Audétat, 2012). Temperatures obtained using this model coincide with estimates obtained using other geothermometers much better than for other models (Acosta et al., 2020). This model is widely used for estimating the crystallization temperature of quartz in different felsic rocks (e.g., Seitz et al., 2018). Model Z20 for Ti partitioning between quartz

[1] Additional materials to the Russian and English on-line versions on sites https://elibrary.ru/ and http://link.springer.com/, respectively, include:
Supplementary 1, ESM_1.xlsx – Position of the studied samples at the Valaam and Lukulunsaari islands.
Supplementary 2, ESM_2.xlsx – Methods.
Supplementary 3, ESM_3.xlsx – Compositions of minerals.
Supplementary 4, ESM_4.xlsx – Chemical composition of the studied samples of the Valaam sill.
Supplementary 5, ESM_5.xlsx –Ti concentration in quartz and calculation of Zr saturation temperature.
Supplementary 6, ESM_6.xlsx – Model 1 of fractional crystallization of ferrogabbro melt calculated in a Melts software.
Supplementary 7, ESM_7.xlsx – Model 2 of fractional crystallization of ferrogabbro melt calculated in Melts software.
Supplementary 8, ESM_8.xlsx – Mass-balance calculation of the fractional crystallization of the ferrogabbro melt.

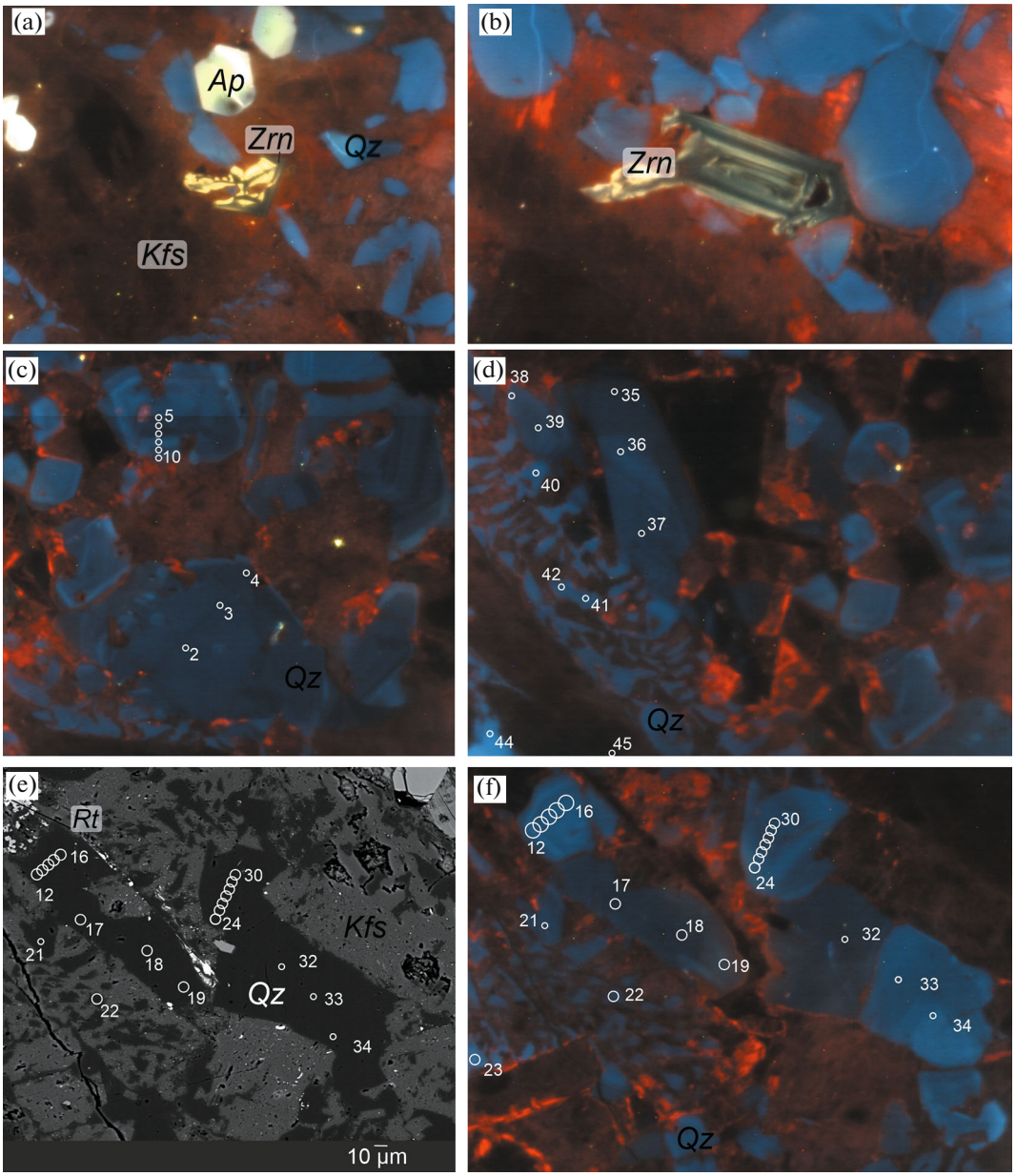

Fig. 4. Microstructures of zircon (a–b, sample 22LD-32a) and quartz (c–f, sample 22LD-25) grains in graphic leucogranites. (a) and (b) CL-images, zircon has yellow luminescence with dark gray veinlets, apatite is greenish yellow. (c), (d), and (f) – CL-images, quartz has blue luminescence, lighter domains have the higher Ti concentrations, isolated grains show well-expressed growth zoning with dark blue cores and light blue peripheral zones; alkaline feldspar shows red luminescence. (c) BSE image in the same area as has shown in (d) in CL rays. Light gray in the left upper corner in (e) and black in (f) is rutile intergrown with quartz. Circles and numerals near them are spots of microprobe analysis and their numbers.

and aluminosilicate melt was calibrated within 700–900°C and 0.5–4 kbar. Errors are – ±25 °C and ±0.2 kbar, respectively. Since quartz in the graphic leucogranites contains rutile inclusions (Fig. 4e), the TiO_2 activity in calculations was taken to be unity. The Zr saturation temperature of felsic melt was calculated using equations from (Borisov and Aranovich, 2019; Boehnke et al., 2013; Gervasoni et al., 2016).

RESULTS

Compositions of Minerals

Compositions of minerals are given in Supplementary 3, ESM_3.

Olivine occurs in ferrogabbro, where it forms separate grains or small clusters consisting of 2–5 euhedral and subhedral grains. Olivine crystals frequently con-

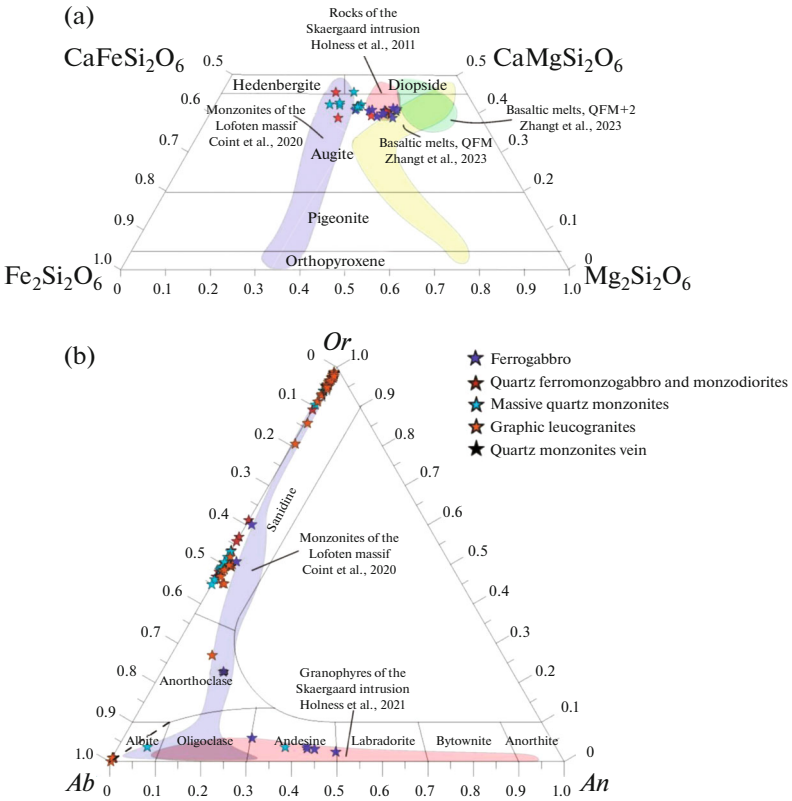

Fig. 5. (a) Compositions of pyroxenes from the rocks of the Valaam sill in the diagram $Fe_2Si_2O_6$–$Mg_2Si_2O_6$–$CaFeSi_2O_6$–$CaMgSi_2O_6$. Compositional fields of pyroxenes from granophyres of the Skaergaard intrusive (Holness et al., 2011), monzosyenites from the Lofoten massif (Coint et al., 2020), and from experimental basaltic melts that crystalized at oxygen fugacity corresponding to QFM and QFM+2 buffers (Zhang et al., 2023) are shown for comparison. (b) Compositions of feldspars from rocks of the Valaam sills in the *An*–*Ab*–*Or* diagram. Compositional fields of feldspars from granophyres of the Skaergaard intrusion (Holness et al., 2011) and monzonites of the Lofoten massif (Coint et al., 2020) are shown for comparison.

tain inclusions of apatite, and more rarely ilmenite. The olivine has a Fe-rich composition (40–42% forsterite), is strongly depleted in Ni (30–80 μg/g) and enriched in Ca (1000–1600 μg/g) and Mn (6200–6300 μg/g).

Clinopyroxene is represented by augite, occurs mainly in ferrogabbro, while its individual grains are also present in the quartz ferromonzogabbro and quartz monzonites. In the ferrogabbro, its grains are mainly unzoned, with thin Fe-rich rims. Magnesian number (Mg# = Mg/(Mg+Fe)×100, mol) of clinopyroxene varies within 44–67, amounting for 46–55 in the quartz monzonite. Concentrations of titanium, aluminum, and manganese in the mineral are sufficiently low, in wt %: TiO_2 0.22–1.1, Al_2O_3 0.61–2.0, MnO 0.32–0.57. Composition of clinopyroxene cores in the ferrogabbro and ferromonzogabbro is close to those of the rocks from the Skaergaard layered massif (Holness et al., 2011); marginal zones and compositions of clinopyroxenes from the quartz monzonites are close to those of clinopyroxene from the monzosyenites of the Lofoten massif (Coint et al., 2020), as seen in Fig. 5a.

Feldspars. Plagioclases are present in the ferrogabbro, quartz ferromonzogabbro, monzodiorite, and quartz monzonite. In these rocks, the central parts of the grains are represented by andesine–oligoclase plagioclase ($An_{0.41–0.28}$) surrounded by distinct rims of K-Na feldspar ($Or_{0.23–0.27}$) with elevated BaO content (1.5 wt %). In the quartz monzonite, these rims are surrounded by K-Na feldspar with high potassium content ($Or_{0.5}$) and low barium content. Alkaline feldspar of similar composition forms separate large crystals in the quartz monzonite and occurs in the contact zones between the ferrogabbro and graphic leucogranites and in the granophyre intergrowths with quartz.

In the graphic leucogranites, the grains of feldspars are mainly represented by spongeous pure K-feldspar and patchy K-Na feldspar ($Or_{0.5}$). Feldspars in the granophyre intergrowths have similar composition. Albite occurs as small xenomorphic crystals together with euhedral quartz.

It should be noted that K-Na feldspars from monzonite of the Lofoten massif (Coint et al., 2020) are enriched in anorthite (Fig. 5b), which likely indicates

the higher crystallization temperatures of alkaline feldspar.

Amphibole and biotite. Hydrous silicate minerals are represented by biotite and amphibole, which are widespread in the massive and vein quartz monzonites and in the graphic leucogranites, and form single grains in the ferrogabbro and quartz monzogabbro. Amphiboles are represented by edenite and ferroedenite (Mg# 89–92), with TiO_2 content varying from 0.6 to 2 wt % and elevated content of F = 1.88 wt %. The Mg# variations from core to rim are insignificant.

Mica is represented by intermediate annite–siderophyllite composition. Quartz monzonite contains higher Mg variety, phlogopite (Mg# 50–65), unlike mica from the graphic leucogranites (Mg# 30–55). Mica shows no zoning within a single grain.

Apatite and titanite. Apatite is characterized by the high F contents (up to 5 wt %), and low Sr and Si concentrations (SrO up to 0.4 wt %, SiO_2 up to 0.6 wt %), and its composition is similar in all rocks. Apatite from the quartz ferromonzogabbro frequently contains annite inclusions.

Titanite frequently replaces ilmenite in the quartz monzonite and graphic leucogranites, as well as in the contact zones of more mafic rocks with graphic leucogranite. Its composition is characterized by the elevated F content (1.3 wt %); Al_2O_3 content in the titanites varies within 1.4–4.1 wt %; some titanites contain insignificant niobium concentrations.

Magnetite and ilmenite. Magnetite is present in all rocks. It is characterized by the chemical variations depending on the petrographic position: in ferrogabbro the magnetite from rims around intergrowths with ilmenite contains 10–12 wt % TiO_2. In the quartz monzonite, the magnetite in the intergrowths with ilmenite is characterized by heterogenous, patchy zoning, high Ti content (17 wt %), and appearance of ilmenite lamellae. In the graphic leucogranites, ilmenite is replaced by titanite, while cracks are filled with high-Ti magnetite (19 wt % TiO_2) enriched in Mn (3.2 wt % MnO). The graphic leucogranites and quartz monzonites contain low-Ti magnetite (1 wt % TiO_2), which could replace or surround the high-Ti magnetites. Ilmenite contains, in wt %: 0.6–0.8 MnO and 0.7–1.1 MgO; fraction of Fe^{3+} is no more than 0.08 apfu.

Zircon has a stable composition with HfO_2 content of 1.0–1.7 wt %.

Chemical Composition of Rocks

Basic and intermediate rocks. Major components. In the olivine ferrogabbro (Supplementary 4, ESM_4), the SiO_2 content varies within 46.59–48.05 wt % (hereinafter, calculated to the water-free basis), the contents of TiO_2 (3.50–3.60 wt %) and total Fe_2O_3 16.90–17.99 wt % are high. Magnesian number of the rocks is 34, total alkali ($Na_2O + K_2O$) content is moderate (4.82–4.89 wt %, Figs. 6, 7a).

In the quartz ferromonzogabbro and quartz monzodiorite, the SiO_2 content varies from 51.80 to 57.10 wt %, Mg# of these rocks is lower than those of ferrogabbro and varies from 25 to 33. The TiO_2 (2.09–2.93 wt %) and Fe_2O_3 (12.60–14.54 wt %) contents are lower than those of ferrogabbro. Total alkalis are 5.38–6.63 wt % (Figs. 6, 7a).

In the quartz monzonite, the SiO_2 content is even higher (57.72–63.35 wt %), but Mg# = 23–34 remains at the same level as that of quartz ferromonzogabbro and monzodiorite. The TiO_2 and total Fe_2O_3 contents are lower (1.13–1.85 and 9.43–12.77 wt %, respectively). Total alkalis are 6.86–8.16 wt % (Figs. 5, 6a).

In all rocks of the Valaam sill, the contents of TiO_2, Al_2O_3, total Fe_2O_3, and MgO decrease with increasing SiO_2 (Figs. 6a–6c, 7), thus demonstrating a "late" segment of the Fenner trend.

Similar trend is observed for the rocks of the AMCG-type Salmi massif (Larin, 2011; Sharkov, 2010), as well as rocks of the AMCG-type Pietkovo massif of the Mazur complex in Poland (Grabarchuk et al., 2023) with an age of 1495–1491 Ma, which is very close to the formation age of the Valaam sill (Fig. 7b).

Felsic rocks. Major components. Vein quartz monzonite (sample 21C-22, see Supplementary 4, ESM_4) contains (in wt %): 61.79 SiO_2, 1.54 TiO_2, 9.70 total Fe_2O_3, 7.35 ($Na_2O + K_2O$), at 37 Mg#. In terms of major componens, it corresponds to the massive monzonite (Figs. 6, 7a). The graphic leucogranites have the elevated SiO_2 content of 73.66–77.69 wt % and are ascribed to the potassic rocks (K_2O/Na_2O = 3.8–6.1) with low CaO content (0.19–0.62 wt %).

Felsic rocks fall in the field of anorogenic alkaline granites (Fig. 8a). They are metaluminous and peralkaline based on the aluminum saturation index A/CNK = 0.88–1.1 ($Al_2O_3/(CaO + Na_2O + K_2O)$, in mol %)), A/NK (Al_2O /($Na_2O + K_2O$), in mol %) = 0.94–1.23 (Fig. 8b). Some rocks fall in the field of ferroan granites based on the Fe index (FeO/(FeO + MgO)) (Frost and Frost, 2011), but have a clear trend toward increasing Mg# (Fig. 8c); all compositions coincide with those of granite veins of the Valaam sill from (Sviridenko and Svetov, 2008).

Basic and intermediate rocks. Trace elements. The fractionated CI (carbonaceous chondrite)-normalized REE patterns of ferrogabbro, quartz ferromonzogabbro, and monzodiorite are similar to that of quartz monzonite: $(La/Lu)_N$ = 10.1–12.7 and a weak positive Eu-anomaly, Eu/Eu* = 1.1–1.2 (Fig. 9). The PM (primitive mantle)-normalized patterns are also similar, with a flat HREE pattern, negative Sr, Nb, Ta, Ti anomalies, and positive Ba and P anomalies. The monzonite has positive U anomaly, while the quartz ferromonzogabbro, a negative U anomaly.

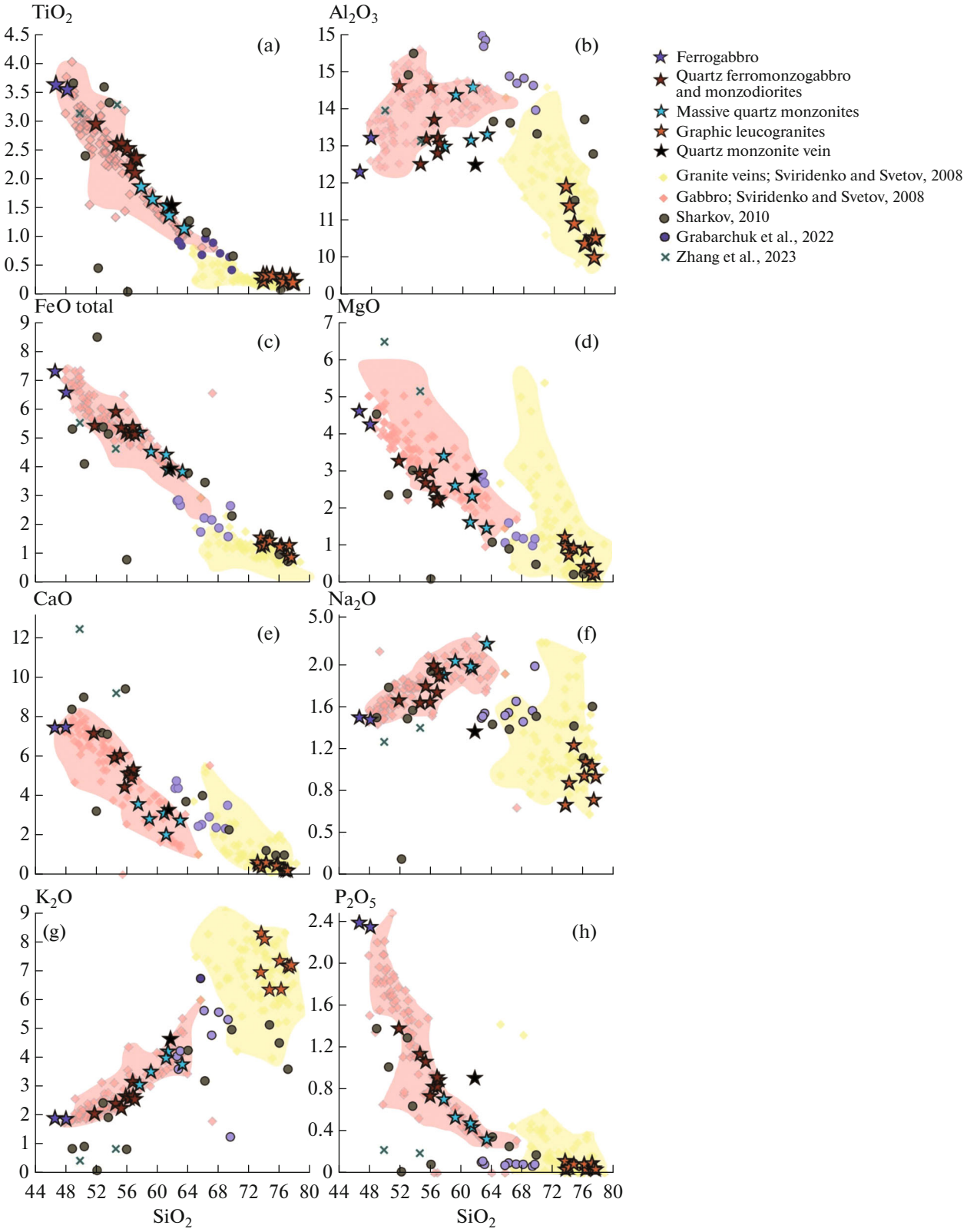

Fig. 6. Harker diagrams for the rocks of the Valaam sill compared to the published compositions of the rocks of the Valaam sill (Sviridenko and Svetov, 2008), rocks of the Salmi massif (Sharkov, 2010), felsic rocks of the AMCG-type Mazur complex with an age of 1.49 Ga (Grabarchuk, 2022), and experimental data on the crystallization of basalts of the Emeishan province (Zhang et al., 2023).

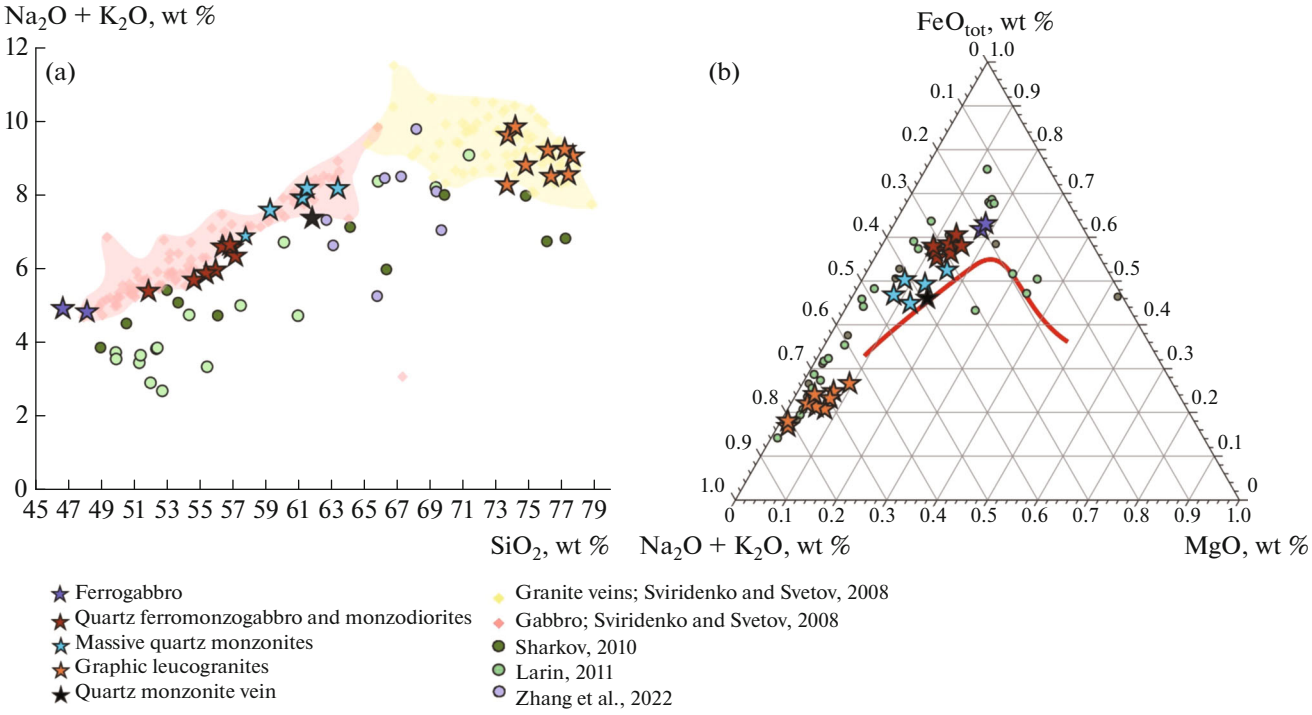

Fig. 7. (a) Diagram SiO_2–($Na_2O + K_2O$) for rocks of the Valaam sill and (b) crystallization trend in the AFM diagram for rocks of the Valaam sill and Salmi massif. Data on the Valaam sill (Sviridenko and Svetov, 2008), Salmi massif (Sharkov, 2010; Larin, 2011), and Mazur complex (Grabarchuk et al., 2023) are shown for comparison.

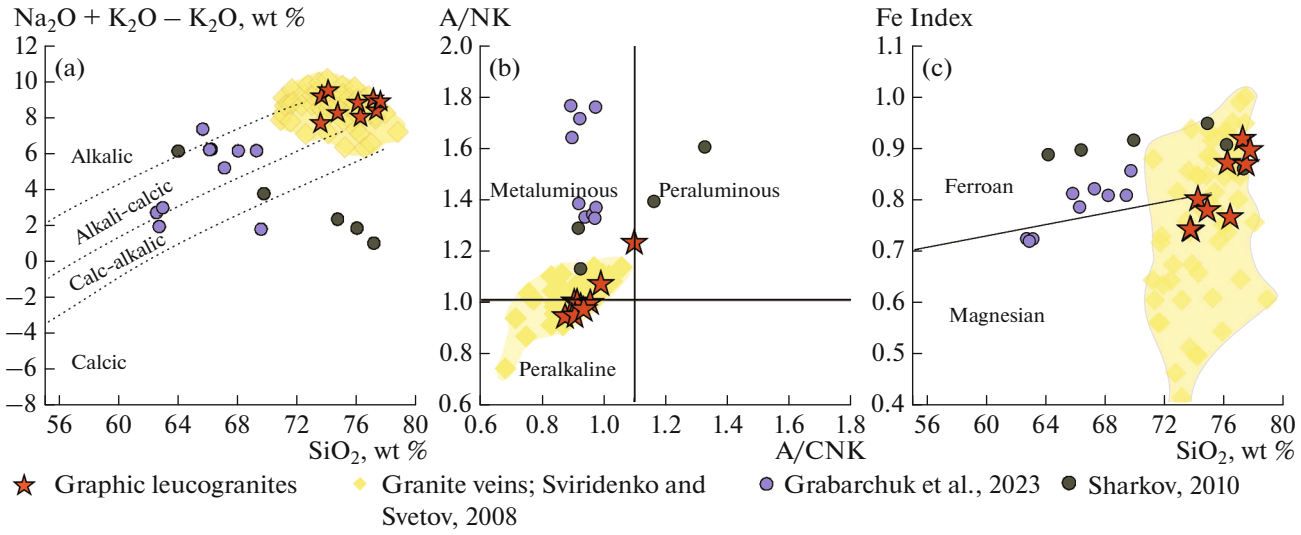

Fig. 8. Characteristics of graphic leucogranites based on: (a) SiO_2 and ($Na_2O + K_2O + CaO$) contents, boundaries between alkalic, alkali-calcic, calc-alkalic, and calc granites after (Frost and Frost, 2011); (b) based on aluminum saturation index A/NK (Al_2O_3/($Na_2O + K_2O$)–A/CNK (Al_2O_3/($CaO + Na_2O + K_2O$), in mol %; and (c) Fe index ($FeO + 0.9Fe_2O_3$)/($FeO + 0.9Fe_2O_3 + MgO$) (Frost et al., 2001) compared to felsic rocks of the Valaam sill (Sviridenko and Svetov, 2008), Salmi massif (Sharkov, 2010), and Pietkovo massif in Poland (Grabarchuk et al., 2023)

Felsic rocks. Trace elements. Vein quartz monzonite (sample 21C-22, see Supplementary 4, ESM_4) compared to the massive quartz monzonite is less enriched in REE, while REE pattern has no Eu anomaly and shows Zr and Hf enrichment (Fig. 9).

The REE patterns of the graphic leucogranites are moderately fractionated $(La/Lu)_N$ = 5.8–12.1. Thereby, LREE are much more fractionated than HREE, have a deep negative Eu anomaly Eu/Eu* = 0.15–0.49. The REE distribution pattern in the graph-

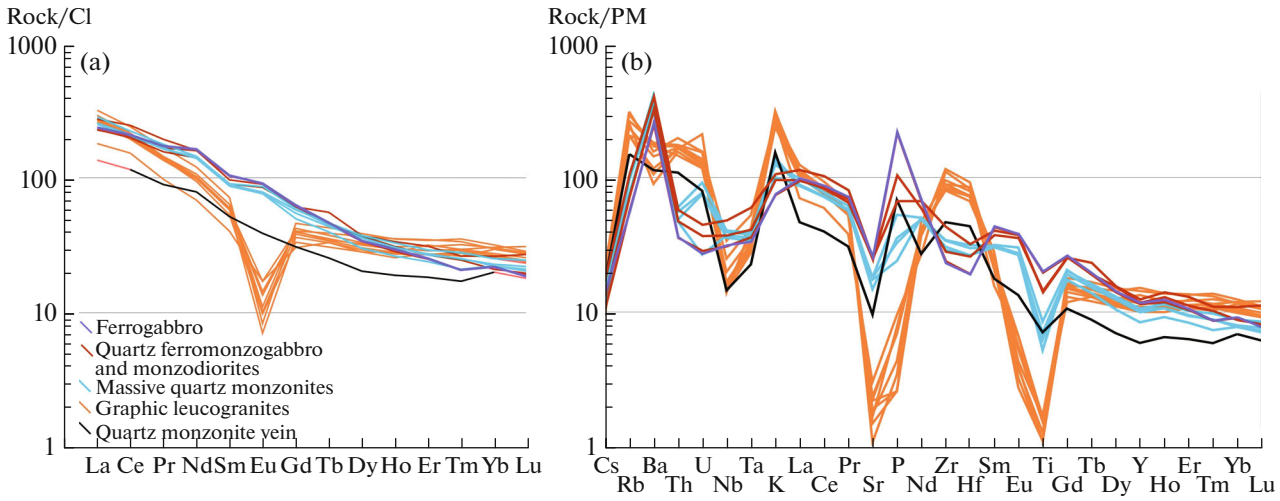

Fig. 9. CI chondrite-normalized REE distribution patterns for the rocks of the Valaam sill (a). Normalizing values for CI chondrite are from (Sun and McDonough, 1989); basic and intermediate rocks have similar distribution patterns with a weak positive anomaly Eu/Eu* = 1.1–1.2, while graphic leucogranites reveal a negative anomaly Eu/Eu* = 0.15–0.49. (b) primitive mantle-normalized trace-element distribution patterns. Normalizing values for primitive mantle are from (Sun and McDonough, 1989). All rocks show negative Sr, Nb, Ta, and Ti anomalies, while ferrogabbro shows a positive P anomaly; graphic leucogranites additionally display positive K, Zr, and Hf anomalies.

ical leucogranites is similar to that of granophyres from the Skaergaard layered massif (Hirschmann, 1992).

The shape of PM-normalized trace-element distribution in leucogranites is typical of A-type granites with enrichment in HFSE, especially in Zr (up to 1141 μg/g) and Hf (up to 23 μg/g) at insignificant negative Nb and Ta anomalies, flat HREE pattern, and deep negative Sr, P, and Ti anomalies.

Thus, the felsic rocks from the Valaam sill differ from its basic–intermediate rocks in the appearance of positive Zr–Hf and Th–U anomalies and deep negative Eu and P anomalies, decreasing HREE fractionation (Fig. 9).

Rb-Sr and Sm-Nd Isotope Composition of Rocks

The Sr-Nd isotope composition was studied in the olivine ferrogabbro, quartz ferromonzogabbro, vein monzonite, and graphic leucogranites of the Valaam sill (Table 1).

These rocks differ in Sr, Rb, and Nd concentrations and their isotopic ratios: Sr concentration is sufficiently low in felsic rocks and moderate in basic rocks, while the Nd content is sufficiently high in basic and intermediate rocks (67–74 ppm) and much lower in the felsic rocks (37–50 ppm); the $^{87}Rb/^{86}Sr$ value is extremely high in the graphic leucogranites (7.89–13.6), high in the vein quartz monzonites (1.29), and moderate in the ferrogabbro (0.2–0.28); the $^{147}Sm/^{144}Nd$ value is slightly higher than in the basic and intermediate rocks (0.122–0.129) and in the vein quartz monzonites (0.130) than in leucogranites (0.112–0.119).

The initial isotope ratio $(^{87}Sr/^{86}Sr)_T$ in the basic and intermediate rocks, and in the leucogranites is 0.7043–0.7066 (Table 1). The Nd isotope composition demonstrates sufficiently high homogeneity and does not depend on the rock type: $\varepsilon_{Nd}(T)$ varies from −9.6 to −11.2. Thereby, the highest and lowest values were obtained for leucogranites, whereas $\varepsilon_{Nd}(T)$ for basic and intermediate rocks fall within the indicated interval.

P-T-fO$_2$ Crystallization Conditions

Zircon. Graphic leucogranites have high Zr content (788–1141 ppm) and contain abundant zircon crystals. Zircon is observed as skeletal crystals (Fig. 4a) and prismatic elongated grains with thin magmatic zoning (Fig. 4b). The morphology of the zircon grains and the absence of xenogenic cores in the cathodoluminescence images point to the rapid crystallization of the zircon grains from the melt. We therefore attempted to estimate the crystallization temperature, assuming melt saturation in Zr. In such an approach, the calculated temperature could differ from the magma temperature (Siégel et al., 2018), but gives an approximate assessment of the system temperature. Calculations using three equations (Borisov and Aranovich, 2019; Boehnke et al., 2013; Gervasoni et al., 2016) yielded similar temperature intervals within 850–1070°C (see Supplementary 5, ESM_5). For further considerations, T = 850–960°C calculated according to the model (Borisov and Aranovich, 2019) was taken as the closest temperature obtained using

Table 1. Sr and Nd isotope compositions in rocks of the Valaam sill

Sample no.	Rock name	Rb, ppm	Sr, ppm	$^{87}Rb/^{86}Sr$	$^{87}Sr/^{86}Sr \pm 2\sigma$	$(^{87}Sr/^{86}Sr)_T$	Sm*, ppm	Nd*, ppm	$^{147}Sm/^{144}Nd$	$^{143}Nd/^{144}Nd \pm 2\sigma$	$\varepsilon_{Nd}(T)$	$T_{(Nd)}DM$, Ma
21C-19	Olivine ferrogabbro	30	459	0.188	0.708202 ± 16	0.70433	15.7	74.2	0.128	0.511443 ± 6	−10.5	
22Ld-37	Quartz ferromonzogabbro	44	499	0.252	0.710115 ± 13	0.70492	13.9	67.0	0.126	0.511447 ± 8	−10.0	2813
22Ld-08	Quartz ferromonzogabbro	38	445	0.249	0.709477 ± 11	0.70436	13.7	65.5	0.127	0.511451 ± 6	−10.1	
22Ld-14	Quartz ferromonzogabbro	80	842	0.274	0.709949 ± 13	0.70431	14.0	65.5	0.129	0.51143 ± 5	−11.0	
22Ld-28	Quartz monzonite	62	368	0.493	0.715689 ± 13	0.70555	13.8	68.4	0.122	0.511365 ± 7	−10.9	2827
21C-22	Vein Quartz monzonite	99	220	1.29	0.731215 ± 17	0.70460	7.9	36.7	0.130	0.511448 ± 11	−10.8	
22Ld-35	Graphic leucogranite	110	40	7.89	0.866778 ± 16	0.70448	8.8	46.2	0.116	0.511372 ± 7	−9.59	2629
21C-13	Graphic leucogranite	136	37	10.7	0.925635 ± 49	0.70577	8.1	43.9	0.112	0.511252 ± 7	−11.2	2710
22Ld-13	Graphic leucogranite	152	32	13.6	0.986319 ± 32	0.70662	9.7	49.7	0.118	0.511368 ± 7	−10.1	2695
22Ld-07	Graphic leucogranite	132	41	9.26	0.894979 ± 700	0.70450	9.0	45.8	0.119	0.511342 ± 6	−10.8	2770

Calculations were made for an age of 1457 Ma (Rämö et al., 2005); * ICP-MS data and $^{147}Sm/^{144}Nd$ ratios calculated using these values; values $(^{87}Sr/^{86}Sr)_T$ were recalculated using constant $^{87}Rb=1.3972\times10^{-11}$ (Villa et al., 2015). Nd model age was calculated after (DePaolo, 1981).

Table 2. *T-P-f*O_2 conditions of crystallization for the rocks of the Valaam sill

Ferrogabbro	Quartz ferromonzogabbro and monzodiorites	Graphic leucogranites
Primocrysts *Cpx* T = 1040–1057°C[1]; P = 250–440 MPa[2]		Melt saturation and crystallization of *Zrn*[5] T = 863–974°C Quartz inclusions in *Kfs*[6] > 903°C Isolated quartz grains T = 793–871°C[6] P = 320–370 MPa[7]
	Ferroedenite[3] T = 683–754°C; P = 50–70 MPa, *Mag* rims around *Ilm*[4] T = 706–784°C; fO_2 =+0.2...−1.2 ΔQFM	Quartz from granophyre aggregate[6] T = 617–704°C
		Quartz from paragenesis with carbonate[6] T = 630–734°C

Models used for calculations: [1] (Putirka, 2008), eqs. 30 and 31; [2] (Putirka, 2008), eq. 33; [3] (Ridolfi, 2021); [4] (Sauerzapf et al., 2008); [5] (Borisov and Aranovich 2019); [6] (Huang, Audétat, 2012); [7] (Zhang et al., 2020).

other mineral sensors, such as quartz inclusions in alkaline feldspar (Table 2), and considered as the near liquidus temperature of the leucogranite melt.

Quartz in the graphic leucogranites is represented by separate isolated grains among granophyre aggregate, crystals intergrown with KFsp in the granophyre aggregate (Fig. 4), and separate crystals associated with carbonate in hydrothermal pockets and veinlets. Quartz is characterized by blue cathodoluminescence (Fig. 4), which indicates its primary magmatic nature (e.g., overview in Shah et al., 2022).

Microstructural features of quartz indicate different conditions of its crystallization. It is most probable that the crystallization of early quartz as individual grains could occur in an intermediate chamber. Taking the minimum temperature of 850°C obtained from the zircon geothermometer, the pressure calculated according to the Ti-in-quartz model Z20 (Zhang et al., 2020) is 320–370 MPa, which is in good agreement with the estimates (220 to 440 MPa) obtained from the clinopyroxene–melt geobarometer (Putirka, 2008) (Table 2). The highest temperature was obtained for quartz inclusion with 360 μg/g Ti in alkaline feldspar (~900°C, it is minimum value without estimated TiO_2 activity).

In cathodoluminescence, separate quartz grains demonstrate reverse zoning with dark blue core, light blue peripheral zone, and blue rim (Figs. 4c, 4d, 4f). The Ti concentration in the core varies from 126 to 174 μg/g, increasing to 174–252 μg/g in the peripheral zone, while rims of large and small grains contain 66–120 μg/g Ti.

Since quartz is associated with rutile in the leucogranites (Fig. 4d), the TiO_2 activity can be taken to be unity. In this case, based on the TitaniQ thermometry, the temperature of quartz formation according to the model HA12 accounted for 790–870°C (Huang and Audétat, 2012).

Quartz from the granophyre aggregate typically demonstrates a homogenous luminescence in identically oriented ingrowths. According to the EPMA data, the Ti content in quartz from the granophyre is 126–156 μg/g in coarse intergrowths. LA-ICP-MS data yield 127–150 μg/g Ti in the quartz from granophyre, which is well consistent with EPMA data.

It is generally accepted that the granophyre microstructures are formed at 0.5–2.0 kbar. However, the main trigger of its crystallization is supercooling rather than decompression (Morgan and London, 2012). The development of ferroedenite after clinopyroxene provides pressure of sill emplacement at ~70 MPa (Table 2). We have taken this pressure estimate of 70 MPa to calculate the crystallization temperature of quartz from the granophyre aggregate using the TitaniQ geothermometer, in which case, the temperature interval of crystallization could be 620–700°C, according to the HA12 model.

Quartz from carbonate-bearing micromiaroles and veinlets contains 113–151 ppm Ti (according to LA-ICP-MS), and its crystallization temperature is estimated at 630–730°C (Huang and Audétat, 2012) or 570–670°C (Zhang et al., 2020).

Other mineral sensors. In the ferrogabbro, clinopyroxene crystallized at 1050°C and 350 MPa (average value) (Putirka, 2008; Table 2).

In the quartz ferromonzogabbro and monzodiorite, the ferroedenite crystals and rims around primocrysts of Fe-rich clinopyroxene (Mg# 46–55) crystallized at 680–750°C and 50–70 MPa (Ridolfi, 2021). Wide magnetite rims forming around ilmenite in these rocks according to the Uvsp-Ilm thermooxybarometer (Sauerzapf et al., 2008) show close temperatures (700–780°C) and slightly varying fO_2 values from +0.2 to −1.2 ΔQFM. Amphibole from intergrowths with ilmenite defines 670–775°C (Ridolfi, 2021); this temperature is close to that obtained with the Fe–Ti oxide sensor (Table 2).

Modeling Melt Crystallization in Melts Software

The Melts software package has been used to model the crystallization of Fe-rich tholeiitic melts (e.g., Toplis and Carroll, 1996; Lino et al., 2023), as well as layered complexes (e.g., VanTongeren et al., 2010; Fischer et al., 2016), and magmas of the AMCG-complexes (e.g., Fred et al., 2020). It has been shown that Melts modeling of the fractional crystallization of tholeiitic melts yields compositions that show immiscibility of Fe- and Si-rich liquids in experiments and natural objects (e.g., Lino et al., 2023). We have used this software package to simulate the crystallization of melts from the Valaam sill.

Parameters of modeling. Ferrogabbro, sample L-10/1, was taken as starting composition for modeling. Our choice was based on the petrography and composition of the rock: it shows no signs of cumulate texture or assimilation of host rocks, and its composition is typical of the sill and corresponds to the standard continental tholeiite.

The crystallization was modelled isobarically at a pressure of 200 MPa, which was chosen based on the minimum estimates (Table 2) and the fact that the same estimates were obtained from mineralogical data for gabbro crystallization leading to the appearance of granophyre in the Bushveld massif (VanTongeren et al., 2010).

Crystallization of the tholeiitic melts strongly depends on the redox conditions and the water content in the melt, as has been shown experimentally (e.g., Toplis and Carroll, 1995; Bocharnikov et al., 2008; Zhang et al., 2023). The absence of hydrous phases amphibole and biotite in the ferrogabbro and their occurrence only in the more evolved quartz monzonite indicates the low water content in the initial melt. Petrography has shown that a magnetite has crystallized after an ilmenite, which for Fe-rich melt indicates the low oxygen fugacity.

Modeling was carried out for two cases: model 1 for dry melt (0.2 wt % H_2O) under reducing conditions (ΔQFM-1) and model 2 for melt with higher water content (1.2 wt % H_2O) under more oxidizing conditions (QFM) (Supplementary 6, 7, ESM_6, 7). These parameters were chosen based on experimental (e.g., Botcharnikov et al., 2008; Toplis and Carroll, 1995; Lino et al., 2023) and modeling (e.g., Fischer et al., 2016; Toplis and Carroll, 1996) data on the crystallization of tholeiitic melts, including data on the liquid immiscibility of silicate melts under relatively dry and reducing conditions.

The influence of water and oxidizing potential on the crystallization trend of tholeiitic melts has been considered in many experiments, which have shown that an increase in water activity and fO_2 will prevent the Fe accumulation in the melt and shift the melt evolution towards the calc-alkaline trend (e.g., Botcharnikov et al., 2008 and review in this work). This is consistent with the difference in model trends obtained (Fig. 10).

In general, the evolution of melt of the Valaam sill is described in the Melts software by a combination of two models: model 1 reproduces the behaviour of Fe and Ti, and model 2 - other components. This difference between Fe and Ti, and other elements could be related to the peculiarities of Melts as noted by (Toplis and Carroll, 1996). The parameters of both models are close, and the rock compositions are mainly between two model trends. The trends are in good agreement with the experimental data (Fig. 10).

The modeling shows that the fractional crystallization could produce composition with SiO_2 contents up to 66 wt %. The 57–66 wt % SiO_2 compositions have TiO_2 = 2.31–1.13 wt % and K_2O 3.1–4.1 wt %, which are close to those of quartz monzonites (2.8 –1.16 and 3.0–4.6 wt %, respectively); modeled and observed contents of other oxides in these rocks are also close (Fig. 10).

Based on the results obtained, the parental melts of the Valaam sill initially had the low water content (0.2–1.2 wt %) and crystallized under relatively reducing conditions with fO_2 between QFM and ΔQFM-1 buffers. It is possible that the variations in these parameters during crystallization were related to the crustal contamination, which caused increasing aH_2O and fO_2.

To test the modeling results, we attempted to obtain the composition of the quartz monzonite from ferrogabbro using mass-balance calculations. The calculations showed that 83% crystallization of ferrogabbro (sample L-10/1) with precipitation of the mineral association $0.16Ol + 0.10Cpx + 0.07Ilm + 0.46Pl + 0.02Kfs + 0.03Ap$ gives a quartz monzonite composition, with melt fraction of 17%, and an error R = 1.69 (see Supplementary 8, ESM_8). Modeling in the Melts software gives a close composition of the crystallizing association: model 1: $0.05Ol + 0.03Opx + 0.16Cpx + 0.06Ilm + 0.42Pl + 0.02Ap$; model 2: $0.06Ol + 0.04Opx + 0.15Cpx + 0.07Ilm + 0.37Pl + 0.02Ap$ and melt fractions of 23% and 28%, respectively (see Supplementary 6, 7, ESM_6, 7).

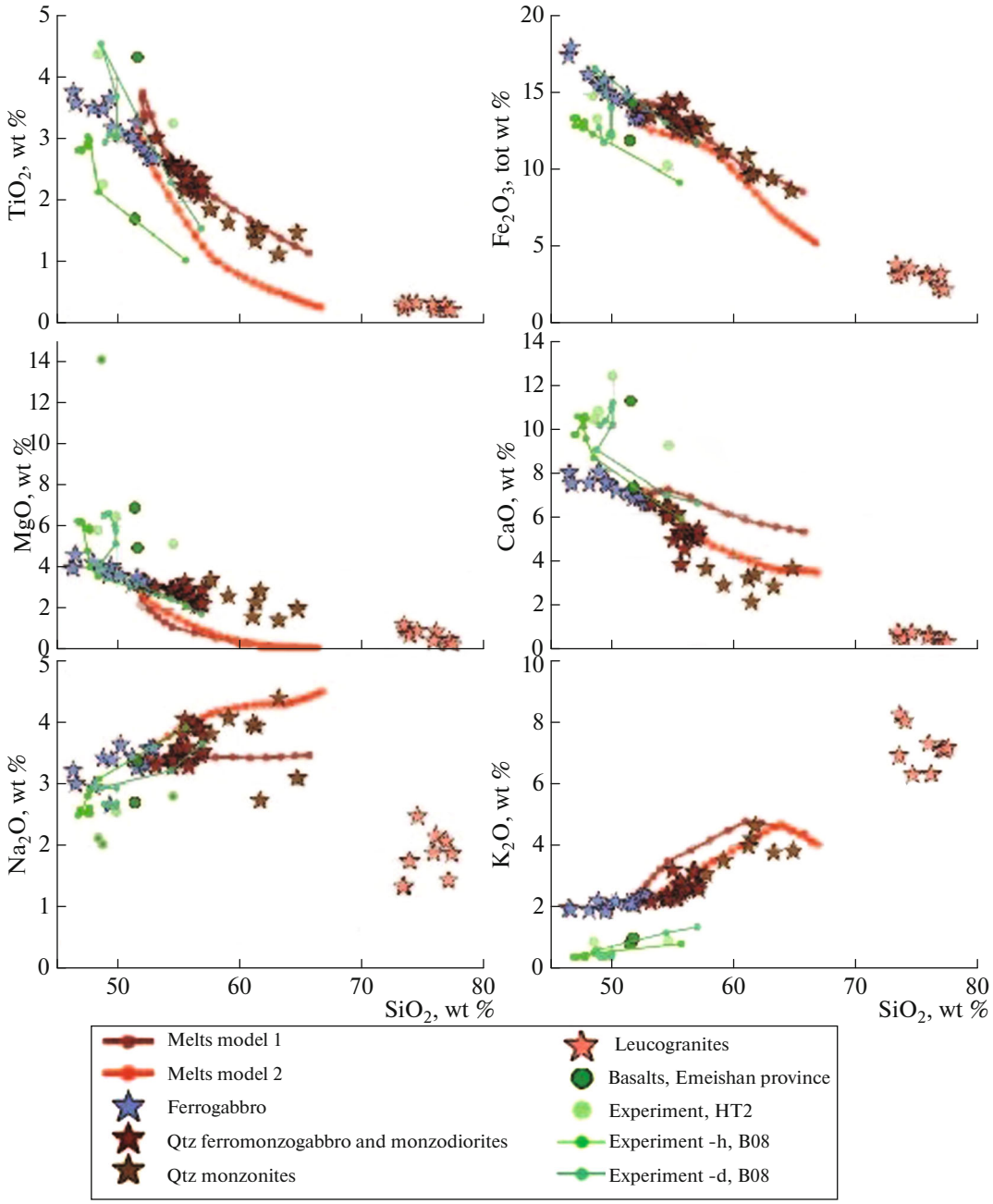

Fig. 10. Modeled liquid lines of descent for the Valaam sill using Melts software shown in the Harker diagrams. Model 1 is shown for dry melt (0.2 wt % H_2O) under reducing conditions (ΔQFM-1) and model 2 for melt with high water content (1.2 wt % H_2O) under more oxidizing conditions (QFM). Asterisks show the melt compositions for the Valaam sill. Also shown are the compositions of high-Ti and low-Ti basalts of the Emeishan Province as an example of typical continental tholeiites and evolution of melts of tholeiitic basalts in experiments (Zhang et al., 2023) and (Botcharnikov et al., 2008) for hydrous (-h) and dry (-d) conditions.

Thus, modeling the fractional crystallization of the ferrogabbro provided the compositions of quartz monzonites, but did not reach the leucogranite composition.

DISCUSSION

Origin of the granite component in the Valaam sill, as well as in many layered intrusions and AMCG-type massifs, remains hotly debatable. It has been proposed

(Frank-Kamenetsky, 1998) that the felsic melts in the Valaam sill are the products of fractional crystallization of basic melts, whereas the leucogranite veins and monzonite lenses were formed by filter pressing. Based on the geochemical similarity of the felsic rocks of the Valaam sill and the Salmi massif, Sviridenko and Svetov (2008) assumed that they were formed through the partial melting of the lower crust under the influence of basic magmas.

In the ε_{Nd}–age diagram (Fig. 11), all the studied rocks of the Valaam sill and the data reported by (Rämö, 1991) fall within the field of the Ladoga block of Paleoproterozoic crust evolution. Granite-gneiss domes in this region represent the fragments of reworked Archean basement, which is confirmed by the low Nd isotope values, ancient Nd model ages, and U-Pb Archean ages of the zircon cores (Konopelko et al., 2005).

The basic and intermediate rocks in the Valaam sill have the Nd isotope composition that is identical to that of the leucogranites (Table 1), and this fact is more consistent with the origin of the felsic rocks through the fractionation of basic melts and/or immiscible separation from Fe-rich basic melts than with melting of crustal sources.

Below we discuss the fractional crystallization in the basic and intermediate melts, possible sources of the felsic melt, including evidence for liquid immiscibility of intermediate melts leading to the appearance of felsic melt, and further evolution of this melt.

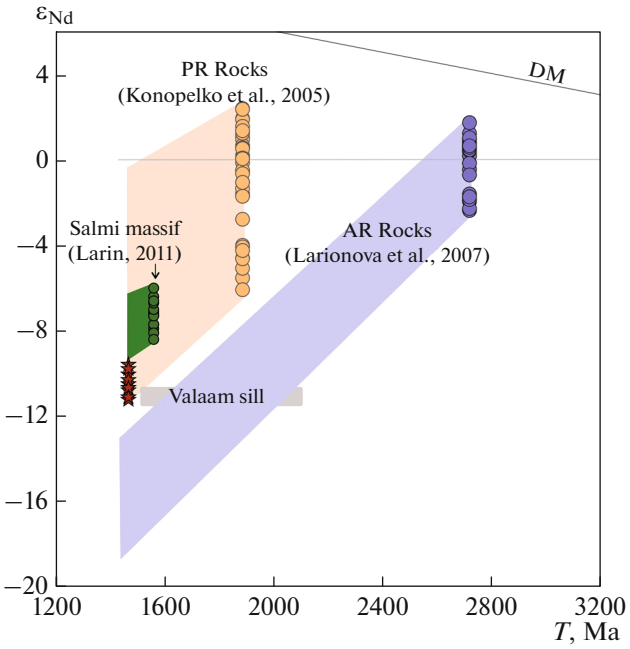

Fig. 11. Diagram ε_{Nd}–age (Ma) for rocks of the Ladoga region. Original data and data from (Ramo, 1991) were used for the Valaam sill, data from (Larin, 2011) were used for the Salmi massif. Pink field shows the evolution trend for the Paleoproterozoic rocks of the North Ladoga region (Konopelko et al., 2005), and violet field shows the evolution trend for the Archean rocks from the western Karelian craton (Larionova et al., 2007).

Fractional Crystallization of Basic and Intermediate Melts and Immiscibility of High-Fe and High-Si Melts

Crystallization Order of Minerals and *T-P-f*O_2 parameters. Geochemical, isotope-geochemical, petrographic, and petrochemical similarity of the rocks of the Valaam sill from the ferrogabbro to quartz monzonites indicates their common origin by fractional crystallization.

Evolved high-Fe compositions of olivine and clinopyroxene, and low-Ca compositions of plagioclase suggest that starting melts were the products of fractional crystallization along the Fenner trend with increasing Fe and decreasing SiO_2.

Apatite was likely the first to crystallize. This was followed by olivine, which contains numerous inclusions of apatite and sometimes ilmenite, and is not intergrown with other minerals. Later, the olivine was overgrown by orthopyroxene (Fig. 3a). After the olivine ceased to crystallize, clinopyroxene and plagioclase were formed. The clinopyroxene crystallized slightly earlier than the plagioclase, as the central parts of the clinopyroxene grains are devoid of plagioclase inclusions, but their rims contain its mutual ingrowths. There are also graphic intergrowths of the clinopyroxene and plagioclase, which likely indicates their co-crystallization. Clinopyroxene and plagioclase contain numerous apatite inclusions.

Eutectoid ilmenite intergrowths with silicate phases, frequently rimmed by magnetite, are characterized by confinement to the clusters of olivine grains. Further crystallization produced ferroedenite, which forms either separate crystals or rims around clinopyroxene. There is also biotite growing on the clinopyroxene or filling interstices, high-Ba feldspar surrounding plagioclase, and late low-Ti magnetite rimming intergrowths of high-Ti magnetite and ilmenite.

Obtained estimates of *T-P-f*O_2 crystallization parameters of the Valaam sill are summarized in Table 2. Previously, the *T-f*O_2 crystallization parameters of melts in the magmatic chamber of the Valaam sill were obtained in (Frank-Kamenetsky, 1998) and correspond to $T = 1100–950$°C and $fO_2 = 10^{-10.5}–10^{-11.5}$ at., i.e., are close to the QFM buffer. Sviridenko (1970) estimated the crystallization conditions of monzonites as 900°C and 10^{-8} atm. It can be seen that these estimates are generaly similar with those obtained by us for the crystallization of basic and intermediate melts (Table 2). Clinopyroxene primocrysts defined a pressure of 350 MPa, which may indicate the position of intermediate chamber in the middle crust, but with allowance for large error of the *Cpx*-melt geobarome-

ter, this reliably indicates crystallization at the middle–upper crustal level. Textural features of the rocks such as the absence of cumulus textures, reaction structures and the sill structure with vaguely expressed layering, suggest that the magma was supplied as crystalline mush at the level of the sill emplacement.

Compositions of the quartz monzonites fall in the immiscibility field. Experiments on the crystallization of ferrobasalts show that their residual melts do not reach the high-SiO_2 compositions typical of layered intrusive granophyres with 72–77 wt % SiO_2. In the experiments (Botcharnikov et al., 2008), the most acidic compositions contained 58 wt % SiO_2, while in the experiments (Toplis and Carroll, 1995) and (Lino et al., 2023) under dry conditions residual melts contained 65–66 wt % SiO_2. Experiments (Zhang et al., 2023) showed that residual melts with SiO_2 54–60 wt % formed during fractional crystallization of ferrobasalts with compositions typical of continental tholeiites at fO_2 = QFM and 1100–1040°C fall into the immiscibility field to unmix into high-SiO_2 and high-Fe liquids. Lino et al. (2023) experimentally demonstrated that immiscibility in the tholeiitic basalts occurs within SiO_2 55–57 wt % at 1010°C. Thus, experiments have shown that the tholeiitic melts within the compositional range of 54–60 wt % SiO_2 at 1010–1100°C are prone to immiscible splitting into high-Fe and high-Si liquids.

The quartz monzonite with SiO_2 contents ranging from 57 to 65 wt % differs from the more basic rocks of the Valaam sill by the high dispersion of all rock-forming oxides, which is well seen in the Harker diagram (Fig. 6). Unsystematic variations in the content of these oxides could be related to the formation of Fe- and Si-rich immiscible melts, which are unevenly distributed among crystalline mush due to the incomplete separation, gravitational settlement of denser Fe-rich melt, and percolation of the acidic melt to the draining channels.

In the Salmi Formation ferrobasalts comagmatic to the Valaam sill, immiscibility between high-SiO_2 and high-Fe melts has been established (Nosova et al., 2022). The presence of felsic glass in the central parts of ferrobasaltic flows has also been pointed out by (Frank-Kamenetsky, 1998). The average SiO_2 content in the felsic glasses is 61.4 ± 7.1 wt % (Nosova et al., 2022), which is well consistent with experiments for alkali-rich tholeiitic compositions. Experimental felsic glasses with Fe-rich globules contained 61–69 wt % SiO_2 (Lino et al., 2023), and 65.8–74.2 wt % SiO_2 (Zhang et al., 2023). Experiments (Charlier and Grove, 2012) showed that when the magma falls into the immiscibility field at 960°C, the acidic liquid could contain 73–76 wt % SiO_2, but at higher temperatures the SiO_2 content will be lower, which is determined by a binodal shape.

In Fig. 12a, we have compared modelled and experimental data on the crystallization of HT2 composition (Zhang et al., 2023) of high-Ti basalts based on the NBO/T parameter, which characterizes the degree of melt polymerization depending on the composition (e.g., Myson, 1986). It is seen that Melts modeling well reproduces experimental data on HT2 basalt (Zhang et al., 2023), and the melt evolution according to model 2 for fO_2 = QFM and H_2O content of 1.2 wt % is very close to these experimental data. All model curves fall in the immiscibility field, intersecting the binodal surface determined at 1040–1050°C (Zhang et al., 2023) or 1020°C (Charlier and Grove, 2012) (Fig. 12).

Microstructures of ilmenite and magnetite. There are three main microstructures of an ilmenite in the basic and intermediate rocks of the Valaam sill. First, ilmenite forms crystals with well-shaped facets, which contain numerous round glass or crystallized polymineral silicate inclusions and sulfide inclusions (type 1). Such crystals are frequently observed in intergrowths with apatite.

Second, the ilmenite forms segregations in the form of intergrowths with silicate (type 2). The ilmenite in these intergrowths has a worm-like, eutectoidal or symplectic shape indicating co- crystallization. The silicate in the intergrowths is represented by clinopyroxene and amphibole, (which may be replaced by chlorite) (Figs. 13a–13e), apatite (Fig. 13g), mineral aggregates of silicate phases and apatite (Fig. 13d), or by feldspar and granophyre (Figs. 13b, 13f). Round sulfide spherules occur as inclusions in or near the ilmenite (Fig. 13c). These ilmenite segregations have round outlines (Fig. 13g) and are 500–1000 μm in size.

Thirdly, the ilmenite–silicate intergrowths are frequently rimmed by magnetite and the symplectite segregations have euhedral outlines due to the growth of the magnetite (Fig. 13a, 13d). The sizes of these type 3 segregations can reach 4000 μm.

Ilmenite crystals of type 1 likely represent primocrysts that entrapped droplets of sulfide liquid during crystallization. The intergrowths of ilmenite with silicate minerals differ in modal composition from the surrounding granophyre matrix (e.g., ilmenite–feldspar or ilmenite–biotite intergrowths do not contain quartz that is typical of granophyre aggregate). The ilmenite–silicate and ilmenite–apatite–silicate intergrowths (type 2) have an appearance typical of sulfide globules in the layered intrusions: polymineral structure, rounded outlines disturbed by the crystallographic shape of the individual minerals (e.g., Barnes et al., 2017, 2023). A sharp boundary between two melts in plutonic conditions is not preserved due to the continuous fractional crystallization and deformation in a crystalline mush. In addition, the lack of clear separation could be related to the low interfacial tension between these two liquids (Veksler et al., 2010).

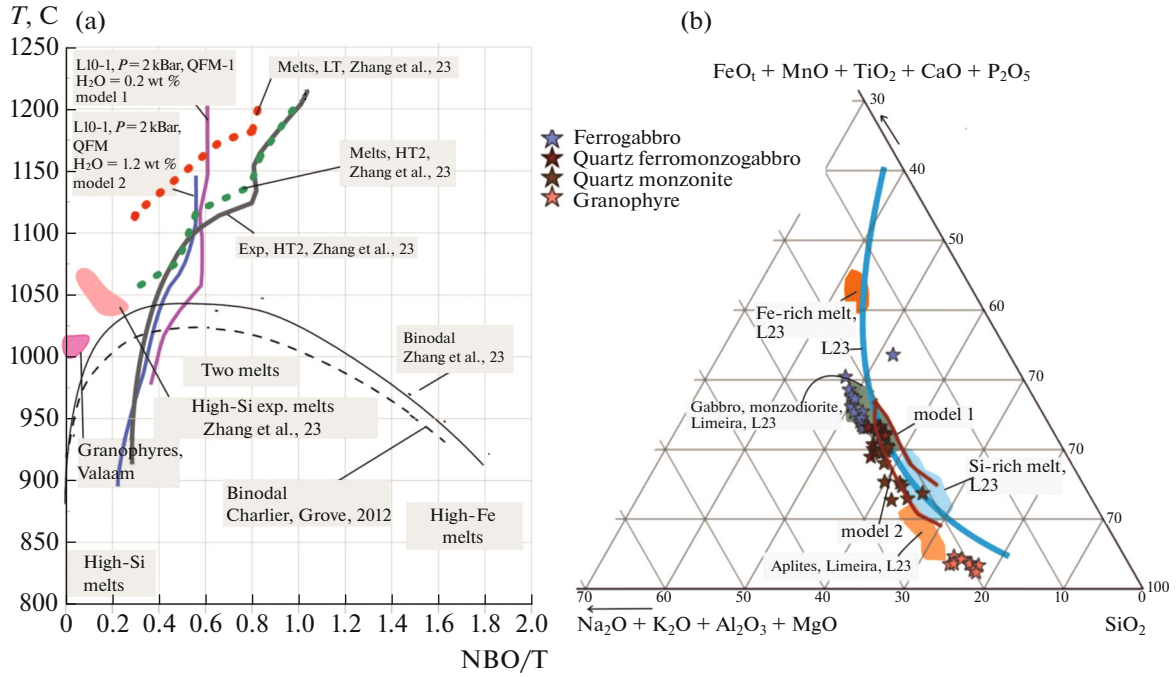

Fig. 12. Comparison of natural and model compositions of melts of the Valaam sill with natural and experimental compositions that were immiscibly split into Si- and Fe-rich melts. (a) models 1 and 2 show the liquid lines of descent for the Valaam sill calculated using Melts software, and lines of experimental high-Ti (green dashed line) and low-Ti (red dashed line) compositions for tholeiitic basalts (Zhang et al., 2023), respectively; gray line was modelled in Melts for high-Ti basalts from experiments (Zhang et al., 2023). Position of binodal surface is shown by a solid line after (Zhang et al., 2023) and dashed line after (Charlier and Grove, 2012). NBO/T is the fraction of non-bridging oxygen in a melt. (b) compositions of rocks of the Valaam sill (asterisks) and the models 1 and 2 for the melt evolution of the Valaam sill calculated in the Rhyolite-Melts software, compositions of Si- (blue field) and Fe- (brown field) rich melts obtained in experiments (Lino et al., 2023), as well as compositions of Limeira massif, which were used as starting compositions in these experiments (gray field) and aplites in this massif (Lino et al., 2023); boundaries of the immiscibility fields (blue line) is shown for alkali-rich tholeiitic basalt (Lino et al., 2023).

The Fe–Ti–P–S-rich composition of type 2 segregations is similar to the composition of the globules in the ferrobasalts with immiscibility microstructures from lava flows in the Ladoga graben. Such globules of Fe–Ti oxide composition (zoned ulvospinel–magnetite–silicate globules, frequently with sulfide core) are embedded in a high-Si–K apo-glass matrix, and frequently they adhere to the apatite crystals (Nosova et al., 2022). Similar globules are well known in tholeiitic basalts: they were formed during the unmixing of Fe-rich silicate melt into high-SiO_2 and high-Fe liquids (Charlier et al., 2013).

The high-Ti magnetite in type 3 segregations forms a rim around the eutectoid intergrowths of ilmenite and silicate phase (Figs. 13a, 13c, 13d), indicating its later origin. The presence of the magnetite rim around ilmenite–silicate intergrowths may point to an increase in fO_2 due to the external impact or, in a closed system, to the relative enrichment of the melt in Fe^{3+} due to the ilmenite crystallization with preferential incorporation of Fe^{2+}.

Non-reactive microstructures similar to types 2 and 3 have been described as "ilmenite-rich intergrowths" in the Skaergaard intrusion and in the Xinjie layered massif in the Emeishan Large Igneous Province; they are considered to be evidence of melt unmixing into Fe- and Si-rich liquids (Holness et al., 2011; Dong et al., 2013). The best evidence for this phenomenon is the occurrence of symplectitic Fe–Ti oxides in granophyre aggregate, which we observed in the Valaam sill (Figs. 13a, 13f).

The assessment of temperature and oxygen fugacity using mineral sensors for the ilmenite-rich segregations (Table 2) indicates the termination of their crystallization with formation of wide magnetite rims at the late magmatic stage at 706–784°C under relatively reducing conditions.

We suggest that the eutectoid ilmenite–magnetite–silicate intergrowths in the holocrystalline rocks of the Valaam sill are analogues of globular immiscible microstructures in basalts.

Evolution of Felsic Melts

Quartz microstructures. Petrographic observations revealed three types of quartz microstructures in the leucogranites: isolated grains and their clusters, granophyre aggregates, and micromiaroles (Fig. 4). Such a diversity of microstructures indicates that leu-

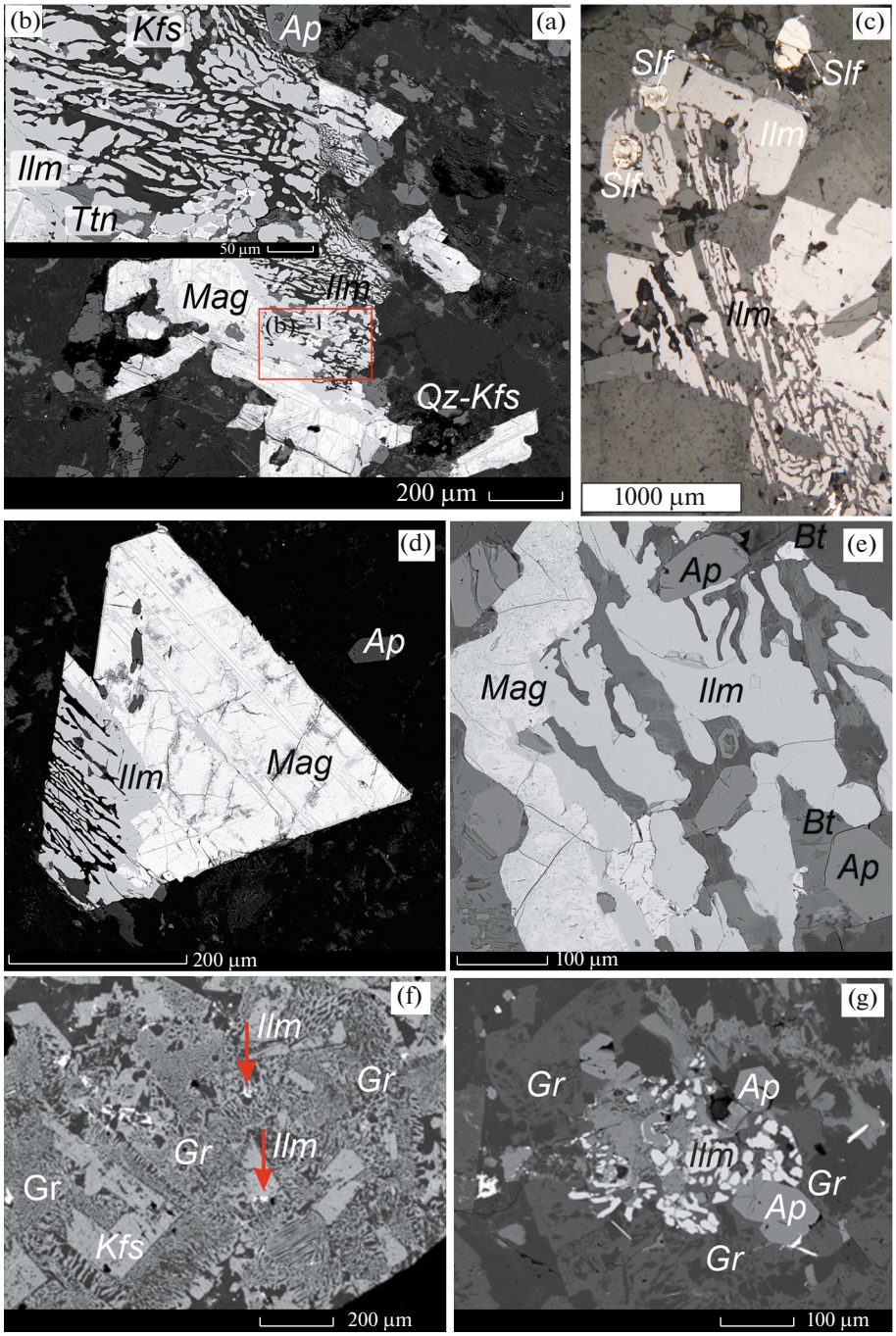

Fig. 13. Microstructures of Fe–Ti-oxides in the quartz monzonites of the Valaam sill: (a) Fe–Ti oxides embedded in the granophyre aggregate, the segregation consists of fine ilmenite–alkali feldspar lamellae and contains inclusions of apatite, ilmenite is partially replaced by titanite, while rim is composed of magnetite; (b) magnified fragments of Fig. (a) distinguished by red box, BSE image; (c) ilmenite–silicate intergrowths in the central part and ilmenite round sulfide inclusions in periphery; one more round sulfide globule is located in the vicinity, in the upper part of the image, reflected light; (d) BSE image of Fe-Ti-oxides as thin intergrowths of ilmenite with alkaline feldspar, rimmed by magnetite with euhedral contours; (e) BSE image of coarse vermicular intergrowhs of ilmenite with amphibole, with magnetite rim; (f) BSE image of ilmenite–silicate intergrowths (shown by red arrow) in the granophyre aggregate; (g) BSE image of ilmenite–apatite intergrowths in a granophyre aggregate.

cogranite crystallization could occur at different depths under varying fluid mode.

The isolated quartz grains were formed in an open space magmatic growth conditions at 733–843°C. The quartz in the granophyre aggregate crystallized under supercooling conditions at 616–694°C (Table 2). The pressure estimated at 70 MPa using ferroedenite rims (Table 2) can be taken as the crystallization pressure of

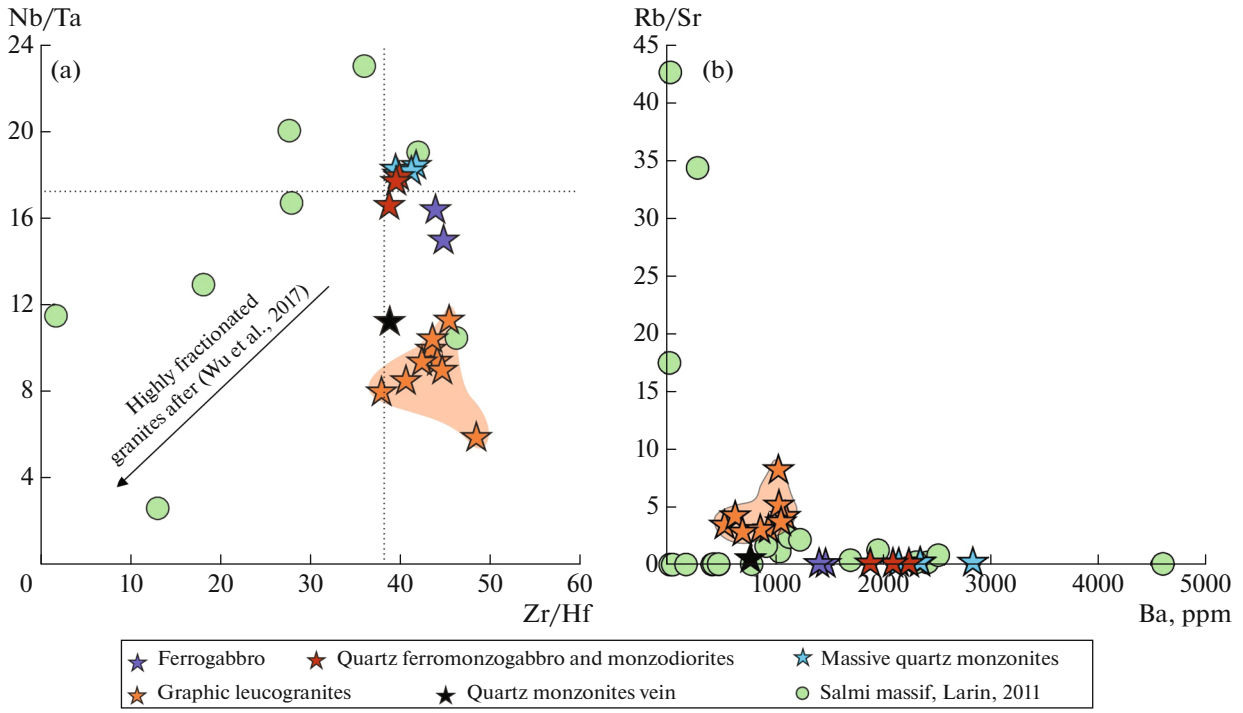

Fig. 14. Diagram Zr/Hf–Nb/Ta (a) and Ba–Rb/Sr (b) for the rocks of the Valaam sill and Salmi massif. Felsic rocks of the Valaam sill fall in the field of weakly fractionated rocks; data on highly fractionated granites (Wu et al., 2017) and on the Salmi massif (Larin, 2011) are shown for comparison.

graphic leucogranites. Our estimate of the leucogranite formation temperature is consistent with experimental data, indicating that the crystallization of granophyre aggregate from hydrous granitic melts requires undercooling up to 200°C (Maneta and Anderson, 2018 and references therein).

The cathodoluminescence images of the quartz grains (Fig. 4) show no traces of core dissolution, which frequently produced an embayment texture in the quartz phenocrysts from volcanic rocks (e.g., Seitz et al., 2018); a continuous zoning points to a relatively calm crystallization conditions without rapid changes.

It is challenging to estimate the solidus of the Valaam sill melts. Based on the estimated crystallization temperatures of clinopyroxene in the quartz monzonite (978–928°C, Table 2), zircon in the granophyres (863–974°C, Table 2), and quartz inclusions in alkaline feldspar (903°C), we can suggest that the solidus of melts of the quartz monzonite composition is ~ 930°C. This estimate is slightly lower than the inferred solidus for melts of the Skaergaard massif: 1040–980°C (Thy et al., 2009), but is comparable to it. The solidus of the granophyre melts was at least 100°C lower, as indicated by petrographic evidence for fluid presence and estimated crystallization temperature of quartz.

Geochemical evidence for leucogranite fractionation. As noted above, Si-rich melts produced by immiscibility in experimental systems have silica contents of 61–69 wt % SiO_2 (Lino et al., 2023) and 65.8–74.2 wt % SiO_2 (Zhang et al., 2023). These contents are lower than those of the graphic leucogranites of the Valaam sill (73–78 wt % SiO_2). It is probable that the felsic melt has fractionated after segregation. We have therefore attempted to find the petrographic and geochemical evidence for the fractionation. Let us consider the vein and massive quartz monzonites with SiO_2 content higher than 57 wt %, i.e. rocks that are more evolved than the possible composition at which liquid immiscibility can occur, based on the results of modeling and experiments (Fig. 12).

In magmatic systems, the Zr/Hf, Nb/Ta, and Y/Ho ratios remain unchangeable during evolution due to the similar geochemical properties of the elements, but fractional crystallization of felsic melts causes their decrease (Wu et al., 2017). The graphic leucogranites show a trend of Nb/Ta shift towards fractionated granites (Fig. 14a). A significant Eu-anomaly in the REE distribution patterns in the leucogranites indicates that they were formed through the extraction from plagioclase–clinopyroxene crystalline mush (ferrogabbro), where Eu^{2+} is partitioned, depleting a residual melt.

In the monzonites, K-feldspar overgrows plagioclase, amphibole, biotite, and clinopyroxene, and these late crystallization processes are expressed to different extent in different rocks. These mineral associations are formed in direct contact with granophyre,

indicating that their crystallization is related to this felsic melt. The monzonites and graphic leucogranites show a slight increase in Rb/Sr and decrease in Ba concentration, likely due to the fractionation of K-feldspar (Fig. 14b).

After partial crystallization, the felsic melts could be extracted from crystalline mush (Gelman et al., 2014) and could have more fractionated composition than at the moment of the immiscible splitting. The difference in melt evolution observed in leucogranite veins, could be related to the different degree of crystallization of these melts prior to their extraction from crystalline mush.

Migration of felsic melt and reactive interaction with host rocks. What happened to the felsic melts after extraction? To understand this, it is important to study the boundaries of graphic leucogranite veins and to determine whether they have interacted with host rocks after extraction.

All leucogranite veins can be subdivided into three types according to their relationship with the host rocks (ferrogabbro).

Thin granite veins without reaction rim at the contact with the host rocks could be formed owing to the hydrorupture of crystalline mush filled with intergranular felsic melt. This was accompanied by the rapid crystallization of the melt, which is supported by the granophyre texture. It should be noted that such veins contain practically no ilmenite–biotite–apatite intergrowths crystallizing from Fe-rich melt. This is likely related to the poor intercalation of Fe-rich melt through the crystalline mush (Holness et al., 2011) or the total low fraction of Fe-rich melt at the late stages of fractional crystallization of the melt in a deep-seated chamber.

The second type of the granite vein is represented by veins with a reaction rim at the contact with the host rock. There is no sharp boundary between the vein and the ferrogabbro, while the granophyre aggregate in the rock is graded into the vein granophyre, indicating that an interstitial liquid was common for both ferrogabbro and vein magmas. In the outercontact zone of the vein, the ferrogabbro shows insignificant changes of mineral composition: overgrowth of amphibole on clinopyroxene, dissolution of plagioclase crystals, and growth of K–Na feldspar rims around them. It should be noted that such changes are also observed in the isolated pockets of granophyre melt, which interacts in a similar manner with primocrysts of plagioclase and clinopyroxene. Such interaction of vein and interstitial melts with primocrysts was caused by the fractional crystallization, resulting in the formation of reactive interstitial liquids (e.g., Peng et al., 2015).

One more type of the leucogranite veins is granophyre pipes (Fig. 2e). They are developed in the Valaam sill (Sviridenko and Svetov, 2008). Similar granophyre pipes have been described in the Skaergaard layered intrusion (Larsen, 2008). The pipes are characterized by the presence of a reaction zone between the pipe and the host ferrogabbro and ferromonzogabbro. In the reaction zone, plagioclase laths are strongly replaced by granophyre quartz and K-feldspar intergrowths, while clinopyroxene crystals are replaced by actinolite–chlorite mixture with mica relics; ilmenite in the ilmenite–magnetite–silicate segregations is replaced by titanite. The contact zone also contains round biotite grains fringed by actinolite and chromite rims (similarly, Rhodes, 1975). Similar granophyres have been described as "ghost" granophyres (Campe, 2021), whose temperature stability range and reactivity increase owing to the high content of fluid component. The high fluid melt is capable of intense metasomatic reworking of the host rocks and the formation of pipes (Figs. 2e, 2f).

Diverse relationships of granophyre veins and interstitial infill with host rocks suggest different migration mechanisms of felsic melt in the crystalline mush of the sill: hydrorupture, filter pressing, and buoyancy of fluid-(over)saturated melt jets.

Late Magmatic Stage and Separation of Fluid Phase

Graphic leucogranite veins contain thin, 1–2 mm, veinlets of quart–K feldspar, quartz–K-feldspar–carbonate, quartz–carbonate, and carbonate composition, and small pockets up to 10 mm across, usually confined to these veinlets and representing their swells (Figs. 3g, 3h). These pockets are characterized by the following zonal structure: leucogranites walls are overgrown by a zone of micrographical quartz–K-feldspar intergrowths. From the walls inwards the general crystalline aggregate separates into individual grains with crystallographic shapes, thus acquiring a finger-like texture (so-called pegmatoid complex, Smirnov, 2015). In the next zone, the individual micrographical clusters are overgrown by K-feldspar, which forms crystals with well-faceted heads directed towards the pocket center (druse complex, Smirnov, 2015). Zone 3 occupies the core of the pocket, which can be filled with quartz or carbonate (Fig. 3g). The zoning of the pockets described above corresponds exactly in structure to the symmetrically zoned miaroles in granite pegmatites (e.g., Jahns and Burnham, 1969; Thomas and Davidson, 2016), which makes it possible to consider them as micromiaroles and directly indicates their crystallization in the presence of aqueous fluid according to the granite scenario (Smirnov, 2015). A transition from a zone of graphical–K-feldspar intergrowths to the druse zone suggests a change of crystallization conditions from the volatile-poor to the volatile-rich system (Thomas and Davidson, 2016).

During the evolution, the granite melt can reach a fluid saturation and the fluid may exsolve into a separate phase; this phenomenon could be triggered either by an increase of volatile concentration in the residual melt up to the saturation due to its partial crystalliza-

tion or by decompression (e.g., Smirnov, 2015). Thus, at the postmagmatic stage, the system consists of three phases: silicate melt, crystals, and fluid mainly of aqueous composition. The fluid phase begins to exsolve as tiny particles dispersed in the melt, which are accumulated as thin films of interstitial, likely moving liquid along the crystal–melt interface. In addition, the fluid can be exsolved as bubbles, that could grow with time and migrate throughout the melt, also merging into jets (Jahns and Burnham, 1969). In this way, the fluid could drain magma to create an interconnected network of microchannels among crystals and the residual melt. Structures corresponding to this process can be exemplified by ocelli in lamprophyres, where silicate–carbonate globules are connected by veinlets of the same composition (e.g., Nosova et al., 2021 and references therein). Interconnected fluid phase creates transport channels (for instance, bubble jets) to provide efficient transfer of matter from one part of the system to another and the growth of phases mainly from components that are well soluble in aqueous fluid (Jahns and Burnham, 1969).

Micromiaroles record a transition to the fluid-bearing system during the crystallization of graphic leucogranites. The crystallization temperature of quartz from the micromiaroles was estimated based on Ti content within 681–584°C (Table 2), which coincides with the upper part of temperature interval of fluid exsolution and of miarolitic pegmatite formation at 700–450°C (Maneta and Anderson, 2018 and references therein) and indicates the supercooling of the melt.

The presence of calcite in the central zone of the micromiaroles and in veinlets requires the consideration of the question of the presence of carbonate in the leucogranite melt. The solubility of CO_2 in a granite melt is sufficiently low (960–1500 μg/g dissolved CO_2, Lowenstern, 2001) and during decompression practically all CO_2 escapes in a gas phase. However, some pegmatites are characterized by the sufficiently high contents of carbonates and sulfates (e.g., Thomas et al., 2011 and references therein), which are dissolved in the associated Na-rich fluids, which could also dissolve significant amounts of SiO_2 and other components (e.g., Kotelnikova and Kotelnikov, 2011).

The quartz–calcite composition of veinlets connecting the micromiaroles suggests that they served as pathways for the migration of silicate–carbonate fluid. The high-T carbonate/bicarbonate fluids enriched in alkali metals could be a good transporting agent for the high field strength elements, including Zr (Savelieva et al., 2014), which can explain the occurrence of zircon grains in the quartz–carbonate veinlets.

CONCLUSIONS

This work presents petrographic, mineralogical, geochemical, and isotope-geochemical studies of graphic leucogranites and host ferrogabbro, quartz ferromonzogabbro, quartz monzodiorite, and quartz monzonite in the Mesoproterozoic Valaam sill in the Ladoga graben. This sill marks the final episode of a long-term (1.67–1.38 Ga) and widespread AMCG-type magmatism of the East European craton.

The sill is characterized by the poorly expressed layering: ferrogabbro is present in the lower part of the sill and grades upward to ferromonzogabbro and quartz monzodiorite, which contain extended interlayers of quartz monzonite. These interlayers become more abundant towards the inferred roof of the sill. The graphic leucogranites (granophyres) form a dense network of veins mainly in the upper part of the sill and are associated with monzonite interlayers.

Experiments and natural observations show that tholeiitic melts with SiO_2 in the range 54–60 wt % at temperatures of 1010–1100°C tend to be separated into high-Fe and high-Si liquids (e.g., Charlier et al., 2013; Charlier and Grove, 2012). We have shown that the compositions of the quartz monzonites are similar to the experimental melts which is split into Fe- and Si-rich liquids. Model calculations have shown that the fractional crystallization could lead to the initial ferrogabbro melt in the immiscibility field.

The ferrogabbro and ferromonzogabbro contain ilmenite–magnetite–silicate intergrowths; similar microstructures have been described as "ilmenite-rich intergrowths" in some layered intrusions as evidence for unmixing between Fe-and Si-rich liquids (Holness et al., 2011; Dong et al., 2013).

Given these facts and the results of modeling of melt evolution and their comparison with experimental data, we suggest that the hypothesis of the origin of graphic leucogranites through liquid immiscibility explains many petrological features of the Valaam sill.

Separation of the high-Si liquid could occur in the middle-crust chamber at ~350 MPa and a temperature no lower than 960°C, as follows from zircon saturation temperature (Table 2), assumed as a liquidus phase for granophyres (Fig. 15b). Quartz crystallized from this melt within a temperature range of 793–871°C. After crystallization with formation of K-feldspar around plagioclase, and amphibole and biotite around clinopyroxene, these melts could be extracted from crystalline mush (Gelman et al., 2014) (Fig. 15c) and have more evolved composition than immediately after their separation from the Fe-rich melt.

Judging from the textural relations between granophyres and host rocks, and the presence of micromiaroles in the granophyre, the leucogranite magma supplying in the sill contained droplets and films of fluid that migrated through the melt. Crystallization of granophyre quartz occurred at 70 MPa and 600–700°C.

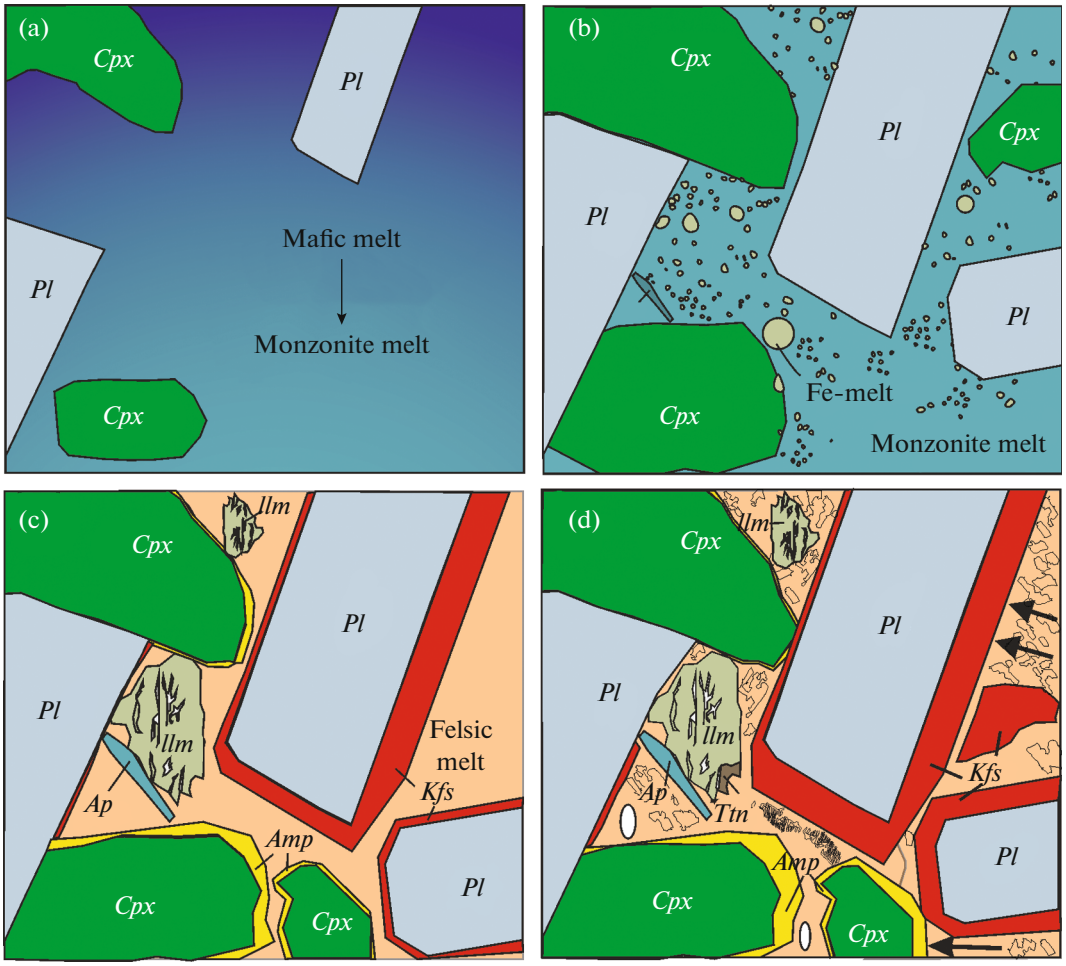

Fig. 15. Scheme of the crystallization order of the primary melt of the Valaam sill: (a) magmatic stage, early crystallization of clinopyroxene and plagioclase, evolution from mafic to monzonitic melt, (b) magmatic stage, continuation of fractional crystallization; immiscible splitting into high-Fe melt as droplets in a matrix of high-Si melt; (c) magmatic stage, continuation of fractional crystallization, formation of clusters of high-Fe melt as ilmenite intergrowths, crystallization of amphibole rim around clinopyroxene and K-feldspar rims around plagioclase from felsic melt; (d) late magmatic stage, formation of granophyre structure, micromiaroles, interaction with host rocks.

Graphic leucogranite (granophyre) in the sill occurs in several structural positions: in interstices in the quartz ferromonzogabbro and monzonite, in veins, and in pipes. Granophyres frequently have reaction relationships with the host rocks. In the reaction rims, accompanying the granophyre in the interstices and in some veins, plagioclase and clinopyroxene primocrysts in the host rock have shown impact from the granophyre. Evidence for the interaction is amphibole rims around clinopyroxene, dissolution texture of plagioclase crystals and their surrounding by alkali feldspar (Fig. 15d). The granophyre in the pipes is accompanied by the reaction zone, where ilmenite is replaced by titanite and plagioclase laths are replaced by granophyre intergrowths, most likely in the fluid presence (Campe, 2021). The quartz–calcite composition of the veinlets connecting the micromiaroles indicates that they served as pathways for the migration of silicate–carbonate fluid.

Our study has shown that when the Fenner-type fractionation trend reaches the final product, ferrogabbro, further evolution will follow a trend of decreasing SiO_2 and Fe contents, which is observed in the layered intrusions and could be related to the incomplete extraction and mixing of immiscible Fe-rich and felsic melts. Such mechanism could be implemented during the formation of the mafic part of the AMCG-type massifs.

SUPPLEMENTARY INFORMATION

The online version contains supplementary material available at https://doi.org/10.1134/S086959112470005X.

ACKNOWLEDGMENTS

We are grateful to M.O. Anosova for help in the LA-ICP-MS determination of Ti content in quartz.

M.A. Yudovskaya and S.Z. Smirnov are thanked for the careful reading of the manuscript and constructive comments. Comments by scientific editor A.V. Samsonov facilitated the improvement of manuscript.

FUNDING

The studies were supported by the Russian Science Foundation (project no. 22-27-00318).

CONFLICT OF INTEREST

The authors of this work declare that they have no conflicts of interest.

REFERENCES

Acosta, M.D., Watkins, J.M., Reed, M.H., et al., Ti-in-quartz: evaluating the role of kinetics in high temperature crystal growth experiments, *Geochim. Cosmochim. Acta,* 2020, vol. 281, pp.149–167.

Amantov, A., Laitakari, I., and Poroshin, Ye., Jotnian and postjotnian sandstones and diabases in the surroundings of the Gulf of Finland. Explanation to the Map of Precambrian basement of Gulf of Finland and surrounding area 1^1 mil, *Geol. Surv. Finland, Spec. Pap.,* 1996, vol. 21, pp. 99–113.

Amelin, Y.V., Larin, A.M., and Tucker, R.D., Chronology of multiphase emplacement of the Salmi rapakivi granite–anorthosite complex, Baltic Shield: implications for magmatic evolution, *Contrib. Mineral. Petrol.,* 1997, vol. 127, pp. 353–368.

Artemieva, I.M. and Shulgin, A., Is the Proterozoic Ladoga rift (SE Baltic Shield) a rift?, *Precambrian Res.,* 2015, vol. 259, pp. 34–42.

Barnes, S.J., Mungall, J.E., Le Vaillant, M., et al., Sulfide–silicate textures in magmatic Ni–Cu–PGE sulfide ore deposits: disseminated and net-textured ores, *Am. Mineral.,* 2017, vol. 102, no. 3, pp. 473–506.

Barnes, S.J., Yudovskaya, M.A., Iacono-Marziano, G., et al., Role of volatiles in intrusion emplacement and sulfide deposition in the supergiant Norilsk–Talnakh Ni–Cu–PGE ore deposits, *Geology,* 2023.
https://doi.org/10.1130/G51359.1

Bindeman, I.N., Brooks, C.K., McBirney, A.R., et al., The low-$\delta^{18}O$ late-stage ferrodiorite magmas in the Skaergaard intrusion: result of liquid immiscibility, thermal metamorphism, or meteoric water incorporation into magma?, *J. Geol.,* 2008, vol. 116, pp. 571–586.

Boehnke, P., Watson, E.B., Trail, D., et al., Zircon saturation re-revisited, *Chem. Geol.,* 2013, vol. 351, pp.324—334.

Bonin, B., A-type granites and related rocks: evolution of a concept, problems and prospects, *Lithos,* 2007, vol. 97, nos. 1–2, pp. 1–29.

Borisov, A. and Aranovich, L., Zircon solubility in silicate melts: new experiments and probability of zircon crystallization in deeply evolved basic melts, *Chem. Geol.,* 2019, vol. 510, pp. 103–112.

Botcharnikov, R.E., Almeev, R.R., Koepke, J., et al., Phase relations and liquid lines of descent in hydrous ferrobasalt - implications for the Skaergaard intrusion and Columbia river flood basalts, *J. Petrol.,* 2008, vol. 49, no. 9, pp. 1687–1727.

Brander, L. and Soderlund, U., Mesoproterozoic (1.47–1.44 Ga) orogenic magmatism in Fennoscandia; baddeleyite U-Pb dating of a suite of massif-type anorthosite in S. Sweden, *Int. J. Earth Sci.,* 2009, vol. 98, no. 3, pp. 499–516.

Campe, C.E., *Ghost Granophyre: A New Texture with Implications for Plagiogranite Differentiation and Ti-in-Quartz Rhermometry, PhD,* Urbana-Champaign: Graduate College of the University of Illinois, 2021.

Charlier, B. and Grove, T.L., Experiments on liquid immiscibility along tholeiitic liquid lines of descent, *Contrib. Mineral. Petrol.,* 2012, vol. 164, no. 1, pp. 27–44.

Charlier, B., Namur, O., and Grove, T.L., Compositional and kinetic controls on liquid immiscibility in ferrobasalt–rhyolite volcanic and plutonic series, *Geochim. Cosmochim. Acta,* 2013, vol. 113, pp. 79–93.

Coint, N., Keiding, J.K., and Ihlen, P.M., Evidence for silicate–liquid immiscibility in monzonites and petrogenesis of associated Fe–Ti–P-rich rocks: example from the Raftsund intrusion, Lofoten, northern Norway, *J. Petrol.,* 2020, vol. 61, no. 4, egaa045.

DePaolo, D.J., Neodymium isotopes in the Colorado Front Range and implications for crust formation and mantle evolution in the Proterozoic, *Nature,* 1981, vol. 291, pp. 193–197.

Dong, H., Xing, C., and Wang, C.Y., Textures and mineral compositions of the Xinjie layered intrusion, SW China: implications for the origin of magnetite and fractionation process of Fe–Ti-rich basaltic magmas, *Geosci. Front.,* 2013, vol. 4, no. 1, pp. 503–515.
https://doi.org/10.1016/j.gsf.2013.01.011

Dyck, B. and Holness, M., Microstructural evidence for convection in high-silica granite, *Geology,* 2022, vol. 50, no. 3, pp. 295–299.

Fenner, C.N., The crystallization of basalts, *Am. J. Sci.,* 1929. Ser. 5, vol. 18, pp. 225–253.

Fischer, L.A., Wang, M., Charlier, B., et al., Immiscible iron- and silica-rich liquids in the upper zone of the Bushveld Complex, *Earth Planet. Sci. Lett.,* 2016, vol. 443, pp. 108–117.

Foden, J., Sossi, P.A., and Wawryk, C.M., Fe isotopes and the contrasting petrogenesis of A-, I- and S-type granite, *Lithos,* 2015, vol. 212–215, pp. 32–44.

Frank-Kamenetsky, D.A., Petrology of Riphean Basites of the Ladoga Region, *Doctoral (Geol.-Min.) Dissertation,* St. Petersburg: St. Petersb. Gos. Univ., 1998.

Fred, R., Heinonen, A., and Heinonen, J.S., Equilibrium crystallization of massif-type anorthosite residual melts: a case study from the 1.64 Ga Ahvenisto complex, southeastern Finland, *Contrib. Mineral. Petrol.,* 2020, vol. 175, no. 9, pp. 1–23.

Frost, C.D. and Frost, B.R., Reduced rapakivi-type granites: the tholeiite connection, *Geology,* 1997, vol. 25, no. 7, pp. 647–650.

Frost, C.D. and Frost, B.R., On ferroan (A-type) granitoids: their compositional variability and modes of origin, *J. Petrol.,* 2011, vol. 52, no. 1, pp. 39–53.

Frost, B.R., Arculus, R.J., Barnes, C.G., et al., A geochemical classification of granitic rocks, *J. Petrol.,* 2001, vol. 42, pp. 2033–2048.

Gelman, S.E., Deering, C.D., Bachmann, O., et al., Identifying the crystal graveyards remaining after large silicic eruptions, *Earth Planet. Sci. Lett.,* 2014, vol. 403, pp. 299–306.

Gervasoni, F., Klemme, S., Rocha-Junior, E.R.V., et al., Zircon saturation in silicate melts: a new and improved model for aluminous and alkaline melts, *Contrib. Mineral. Petrol.,* 2016, vol. 171, no. 3, pp. 1–12.

Grabarczyk, A., Wiszniewska, J., Krzeminska, E., et al., A new A-type granitoid occurrence in southernmost Fennoscandia: geochemistry, age and origin of rapakivi-type quartz monzonite from the Pietkowo IG1 borehole, NE Poland, *Mineral. Petrol.,* 2023, vol. 117, no. 1, pp. 1–25.

Hirschmann, M., Origin of the transgressive granophyres from the layered series of the Skaergaard intrusion, East Greenland, *J. Volcanol. Geotherm. Res.,* 1992, vol. 52, nos. 1–3, pp. 185–207.

Holness, M.B., Stripp, G., Humphreys, M.C.S., et al., Silicate liquid immiscibility within the crystal mush: late-stage magmatic microstructures in the Skaergaard intrusion, East Greenland, *J. Petrol.,* 2011, vol. 52, no. 1, pp. 175–222.

Honour, V.C., Holness, M.B., Partridge, J.L., et al., Microstructural evolution of silicate immiscible liquids in ferrobasalts, *Contrib. Mineral. Petrol.,* 2019, vol. 174, no. 9, pp. 1–24.

Huang, R. and Audétat, A., The titanium-in-quartz (TitaniQ) thermobarometer: a critical examination and re-calibration, *Geochim. Cosmochim. Acta,* 2012, vol. 84, pp. 75–89.

Jahns, R.H. and Burnham, C.W., Experimental studies of pegmatite genesis: I. A model for the derivation and crystallization of granitic pegmatites, *Econ. Geol.,* 1969, vol. 64, no. 8, pp. 843–864.

Jakobsen, J.K., Veksler, I.V., Tegner, C., et al., Immiscible iron- and silica-rich melts in basalts petrogenesis documented in the Skaergaard intrusion, *Geology,* 2005, vol. 33, no. 11, pp. 885–888.

Johansson, A., Bingen, B., Huhma, H., et al., A geochronological review of magmatism along the external margin of Columbia and in the Grenville-age orogens forming the core of Rodinia, *Precambrian Res.,* 2022, vol. 371, p. 106463.
https://doi.org/10.1016/j.precamres.2021.106463

Karandashev, V.K., Khvostikov, V.A., Nosenko, S.V., and Burmii, Z.P., Stable highly enriched isotopes in routine analysis of rocks, soils, grounds, and sediments by ICP-MS, *Inorg. Mater.,* 2017, vol. 53, pp. 1432–1441.

Konopelko, D., Savatenkov, V., Glebovitsky, V., et al., Nd isotope variation across the Archaean–Proterozoic boundary in the north Ladoga area, Russian Karelia, *GFF,* 2005, vol. 127, no. 2, pp. 115–122.

Kotel'nikova, Z.A. and Kotel'nikov A.R. The phase state of NaF-containing fluid at 700°C and 1, 2, and 3 kbar (from the results of study of synthetic fluid inclusions in quartz), *Russ. Geol. Geophys.,* 2011, vol. 52, no. 11, pp. 1298–1309.

Kuptsova, A.V., Khudoley, A.K., Devis, V.I., et al., Age and provenances of sandstones from the Riphean Priozersk and Salmi formations in the Eastern Pasha–Ladoga Basin (southern margin of the Baltic Shield), *Stratigraphy. Geol. Correlation,* 2011, vol. 19, no. 2, pp. 125–140.

Larin, A.M., *Granity rapakivi i assotsiiruyushchie porody* (Granite Rapakivi and Associated Rocks), St. Petersburg: Nauka, 2011.

Larionova, Yu.O., Samsonov, A.V., and Shatagin, K.N., Sources of Archean sanukitoids (high-mg subalkaline granitoids) in the Karelian Craton: Sm-Nd and Rb-Sr isotopic-geochemical evidence, *Petrology,* 2007, vol. 15, no. 6, pp. 530–550.

Larsen, B.R., Syn-magmatic granophyric-rich pipes in the Skaergaard intrusion, East Greenland: implications for cross-cumulus melt transfer during layered gabbro formation, *Int. Geol. Congress,* Oslo, 2008. https://gsi.ir/en/articles/9172/

Latypov, R., Chistyakova, S., Costin, G., et al., Monomineralic anorthosites in layered intrusions are indicators of the magma chamber replenishment by plagioclase-only-saturated melts, *Sci. Rept.,* 2020, vol. 10, no. 1, pp. 1–14.

Lesher, C.E., Brown, E.L., Barfod, G.H., et al., Iron isotope systematics of the Skaergaard intrusion and implications for its liquid line of descent, *J. Petrol.,* 2023, vol. 64, no. 8.
https://doi.org/10.1093/petrology/egad053

Lino, L.M., Carvalho, P.R., Vlach, S.R.F., et al., Evidence for silicate liquid immiscibility in recharging, alkali-rich tholeiitic systems: the role of unmixing in the petrogenesis of intermediate, layered plutonic bodies and bimodal volcanic suites, *Lithos,* 2023, vol. 450–451, pp. 107–193.
https://doi.org/10.1016/j.lithos.2023.107193

Lowenstern, J.B., Carbon dioxide in magmas and implications for hydrothermal systems, *Mineral. Deposita,* 2001, vol. 36, no. 6, pp. 490–502.

Lubnina, N.V., Mertanen, S., Soderlund, U., et al., A new key pole for the East European Craton at 1452 Ma: palaeomagnetic and geochronological constraints from mafic rocks in the Lake Ladoga region (Russian Karelia), *Precambrian Res.,* 2010, vol. 183, no. 3, pp. 442–462.

Maksimov, A.V., Bogdanov, Yu.B., Voinova, O.A., et al., *Gosudarstvennaya geologicheskaya karta Rossiiskoi Federatsii. Masshtab 1:1 000 000 (tret'e pokolenie). Seriya Baltiiskaya. List P-(35),36. Petrozavodsk. Ob"yasnitel'naya zapiska* (State Geological Map of the Russian Federation. Scale 1:1 000 000 (Third Generation). Baltiiskaya Series. Sheet P-(35),36. Petrozavodsk. Explanatory Note), St. Petersburg: Kartograficheskaya fabrika VSEGEI, 2015.

Maneta, V. and Anderson, A.J., Monitoring the crystallization of water-saturated granitic melts in real time using the hydrothermal diamond anvil cell, *Contrib. Mineral. Petrol.,* 2018, vol. 173, no. 10, p. Ñ. 0.

Mathez, E.A., Large-scale liquid immiscibility at the top of the Bushveld Complex, South Africa, *Geology,* 2012, vol. 40, no. 6, pp. 491–494.

McBirney, A.R., The Skaergaard intrusion, *Dev. Petrol.,* 1996, vol. 15, pp. 147–180.

McLelland, J.M., Selleck, B.W., Hamilton, M.A., et al., Late- to post-tectonic setting of some major Proterozoic anorthosite–mangerite–charnockite–granite (AMCG) suites, *Can. Mineral.,* 2010, vol. 48, no. 4, pp. 729–750.

Morgan, G.B. and London, D., Process of granophyre crystallization in the Long Mountain Granite, southern Oklahoma, *Geo-Mar. Lett.,* 2012, vol. 124, nos. 7–8, pp. 1251–1261.

Namur, O., Charlier, B., Toplis, M.J., et al., Crystallization sequence and magma chamber processes in the ferrobasaltic Sept Iles layered intrusion, Canada, *J. Petrol.,* 2010, vol. 51, no. 6, pp. 1203–1236.

Neymark, L.A., Amelin Yu.A., and Larin, A.M., Pb-Nd-Sr isotopic and geochemical constraints on the origin of the 1.54-1.56 Ga Salmi rapakivi granite–anorthosite batholith (Karelia, Russia), *Mineral. Petrol.,* 1994, vol. 50, nos. 1–3, pp. 173–193.

Nosova, A.A., Sazonova, L.V., Kargin, A.V., et al., Mineralogy and geochemistry of ocelli in the damtjernite dykes and sills, Chadobets Uplift, Siberian Craton: evidence of the fluid-lamprophyric magma interaction, *Minerals,* 2021, vol. 11, no. 7, pp. 1–24.
https://doi.org/10.3390/min11070724

Nosova, A.A., Lebedeva, N.M., Sazonova, L.V., et al., Immiscibility between Fe- and Si-rich silicate melts in Mesoproterozoic ferrobasalt of the Ladoga graben, Karelia, Russia, *Dokl. Earth Sci.,* 2022, vol. 505, no. 2, pp. 517–523.

Peng, P., Wang, X., Lai, Y., et al., Large-scale liquid immiscibility and fractional crystallization in the 1780 Ma Taihang dyke swarm: implications for genesis of the bimodal Xiong'er volcanic province, *Lithos,* 2015, vol. 236, pp. 106–122.

Putirka, K.D., Thermometers and barometers for volcanic systems, *Rev. Mineral. Geochem.,* 2008, vol. 69, pp. 61–120.
https://doi.org/10.2138/rmg.2008.69.3

Rämö, O.T., *Petrogenesis of the Proterozoic rapakivi granites and related rocks of southeastern Fennoscandia: Nd and Pb isotopic and general geochemical constraints*, *Geol. Surv. Finland,* 1991.

Rämö, O.T., Mänttäri, I., Vaasjoki, M., et al., Age and significance of Mesoproterozoic CFB magmatism, Lake Ladoga region, NW Russia, *Geol. Soc. Amer. Abstract Programs,* 2001, vol. 33, p. 6.

Rhodes, R.C., Bushveld granophyre in the Stavoren tin district, Transvaal, *South Afr. J. Geol.,* 1975, vol. 78, no. 1, pp. 71–74.

Ridolfi, F., Renzulli, A., and Puerini, M., Stability and chemical equilibrium of amphibole in calc-alkaline magmas: an overview, new thermobarometric formulations and application to subduction-related volcanoes, *Contrib. Mineral. Petrol.,* 2010, vol. 160, pp. 45–66.

Ridolfi, F., Amp-TB2: an updated model for calcic amphibole thermobarometry, *Minerals,* 2021, vol. 11, no. 3, p. 324.

Sauerzapf, U., Lattard, D., Burchard, M., and Engelmann, R., The titanomagnetite-ilmenite equilibrium: new experimental data and thermo-oxybarometric application to the crystallization of basic to intermediate rocks, *J. Petrol.,* 2008, vol. 49, no. 6, pp. 1161–1185.

Savel'eva, V.B., Bazarova, E.P., Sharygin, V.V., and Karmanov, N.S., Zircon—quartz—calcite segregations in the carbonate—alaline metasomatites of the western Baikal region and their petrogenetic significance, *Zap. Ross. Mineral. O-va,* 2014, vol. 143, no. 5, pp. 1–16.

Seitz, S., Putlitz, B., Baumgartner, L., et al., A nanoSIMS investigation on timescales recorded in volcanic quartz from the silicic Chon Aike province (Patagonia), *Front. Earth Sci.,* 2018, vol. 6, pp. 1–19.

Shah, S.A., Shao, Y., Zhang, Y., et al., Texture and trace element geochemistry of quartz: a review, *Minerals,* 2022, vol. 12, no. 8, pp. 1–25.

Sharkov, E.V., Middle-Proterozoic anorthosite–rapakivi granite complexes: an example of within-plate magmatism in abnormally thick crust: evidence from the East European Craton, *Precambrian Res.,* 2010, vol. 183, no. 4, pp. 689–700.

Shellnutt, J.G., Zhou, M.F., and Zellmer, G.F., The role of fe-ti oxide crystallization in the formation of A-type granitoids with implications for the Daly gap: an example from the Permian Baima igneous complex, SW China, *Chem. Geol.,* 2009, vol. 259, nos. 3–4, pp. 204–217.

Siegel, C., Bryan, S.E., Allen, C.M., et al., Use and abuse of zircon-based thermometers: a critical review and a recommended approach to identify antecrystic zircons, *Earth-Sci. Rev.,* 2018, vol. 176, pp. 87–116.

Skursch, O., Tegner, C., Lesher, C.E., et al., Two expressions of the transition from mafic cumulates to granitoids in the Bushveld complex, South Africa: examples from the western and eastern limbs, *Lithos,* 2020, vol. 372-373, p. 105671.

Smirnov S.Z. The fluid regime of crystallization of water-saturated granitic and pegmatitic magmas: a physicochemical analysis, *Russ. Geol. Geophys.*, 2015, vol. 56, no. 9, pp. 1292–1307.

Stepanov, K.I., Zhitnikova, I.A., Mikhailova, D.V., et al., *Gosudarstvennaya geologicheskaya karta SSSR masshtaba 1:200000. Seriya Karel'skaya. Listy R-35-XXIV, R-36-XIX (Sortavala). Ob"yasnitel'naya zapiska* (State Geological Map of the USSR on a Scale 1:200 000. Karelian Series. Sheets R-35-XXIV, R-36-XIX (Sortavala). Explanatory Note), St. Petersburg, 2004. Sun, S. and McDonough, W., Chemical and isotopic systematics of oceanic basalts: implications for mantle composition and processes // Geol. Soc. London: Spec. Publ., 1989, vol. 42, pp. 313–345.
https://doi.org/10.1144/GSL.SP.1989.042.01.19

Sviridenko, L.P., On problem of genesis of rapakivi and other potassium granites, *Petrologiya i strukturnyi analiz kristallicheskikh obrazovanii* (Petrology and Structural Analysis of Crystalline Rocks), Leningrad: Nauka, 1970, pp. 152–156.

Sviridenko, L.P. and Svetov, A.P., *Valaamskii sill gabbrodoleritov i geodinamika kotloviny Ladozhskogo ozera* (Valaam Gabbrodolerite Sill and Geodynamics of the Lake Ladoga Basin), Petrozavodsk: Karel. NTs RAN, 2008.

Thomas, R., Davidson, P., and Schmidt, C., Extreme alkali bicarbonate- and carbonaterich fluid inclusions in granite pegmatite from the Precambrian Ronne granite, Bornholm Island, Denmark, *Contrib. Mineral. Petrol.,* 2011, vol. 161, pp. 315–329.

Thomas, R. and Davidson, P., Revisiting complete miscibility between silicate melts and hydrous fluids, and the extreme enrichment of some elements in the supercritical state—consequences for the formation of pegmatites and ore deposits, *Ore Geol. Rev.,* 2016, vol. 72, pp. 1088–1101.

Thy, P., Lesher, C.E., and Tegner, C., The Skaergaard liquid line of descent revisited, *Contrib. Mineral. Petrol.,* 2009, vol. 157, pp. 735–747.
https://doi.org/10.1007/s00410-008-0361-6

Toplis, M.J. and Carroll, M.R., An experimental study of the influence of oxygen fugacity on Fe–Ti oxide stability,

phase relations, and mineral–melt equilibria in ferro-basaltic systems, *J. Petrol.,* 1995, vol. 36, no. 5, pp. 1137–1170.

Toplis, M.J. and Carroll, M.R., Differentiation of ferro-basaltic magmas under conditions open and closed to oxygen: implications for the Skaergaard intrusion and other natural systems, *J. Petrol.,* 1996, vol. 37, no. 4, pp. 837–858.

Troll, V.R., Nicoll, G.R., Ellam, R.M., et al., Petrogenesis of the Loch Ba ring-dyke and Centre 3 granites, Isle of Mull, Scotland, *Contrib. Mineral. Petrol.,* 2021, vol. 176, no. 2, pp. 1–22.

Van Achterbergh, E., Ryan, C., Jackson, S., and Griffin, W., Data reduction software for LA-ICP-MS laser ablation ICP-MS in the earth sciences–-principles and applications, *Mineral. Ass. Canada, Short Courses,* 2001, vol. 29, pp. 239–224.

Vantongeren, J.A., Mathez, E.A., and Kelemen, P.B., A felsic end to bushveld differentiation, *J. Petrol.,* 2010, vol. 51, no. 9, pp. 1891–1912.

Veksler, I.V., Kahn, J., Franz, G., and Dingwell, D.B., Interfacial tension between immiscible liquids in the system K_2O–FeO–Fe_2O_3–Al_2O_3–SiO_2 and implications for the kinetics of silicate melt unmixing, *Am. Mineral.,* 2010, vol. 95, pp. 1679–1685.

Villa, I.M., Bievre, P.De., Holden, N.E., et al., IUPAC-IUGS recommendation on the half life of ^{87}Rb, *Geochim. Cosmochim. Acta,* 2015, vol. 164, pp. 382–385.

Wager, L. and Brown, G., *Layered Igneous Rocks,* Edinburgh–London: Oliver and Boyd, 1968.

Wu, F.Y., Liu, X.C., Ji, W.Q., et al., Highly fractionated granites: recognition and research, *Sci. China Earth Sci.,* 2017, vol. 60, no. 7, pp. 1201–1219.

Zhang, C., Li, X., Almeev, R.R., et al., Ti-in-quartz thermobarometry and TiO_2 solubility in rhyolitic melts: new experiments and parametrization, *Earth Planet. Sci. Lett.,* 2020, vol. 538, p. 116213.

Zhang, Y., Namur, O., and Charlier, B., Experimental study of high-Ti and low-Ti basalts: liquid lines of descent and silicate liquid immiscibility in large igneous provinces, *Contrib. Mineral. Petrol.,* 2023, vol. 178, no. 1, pp. 1–24.

Zhu, D., Bao, H., and Liu, Y., Non-traditional stable isotope behaviors in immiscible silica–melts in a mafic magma chamber, *Sci. Rept.,* 2015, vol. 5, pp. 1–10.